A cell-type-resolved human brain atlas of microRNAs and tRNA fragments

Serafima Dubnov[1], Lihen Laski[2], Ido Zchut[2], Ofek Avidan[2], Estelle R. Bennett[2], David S. Greenberg[2], Adi Tujerman[2], Mor Nitzan,[3,4,5], Iddo Paldor[6*], Hermona Soreq[1,2*]

1. The Edmond & Lily Safra Center for Brain Sciences, The Hebrew University of Jerusalem, Jerusalem, Israel.
2. The Alexander Silberman Institute of Life Sciences, The Hebrew University of Jerusalem, Jerusalem, Israel.
3. The School of Computer Science and Engineering, The Hebrew University of Jerusalem, Jerusalem, Israel.
4. The Racah Institute of Physics, The Hebrew University of Jerusalem, Jerusalem, Israel.
5. The Faculty of Medicine, The Hebrew University of Jerusalem, Jerusalem, Israel.
6. The Neurosurgery Department, Shaare Zedek Medical Center, Jerusalem, Israel.

*These authors contributed equally as senior authors.

Abstract

MicroRNAs (miRs) and transfer RNA fragments (tRFs) regulate multiple brain processes ranging from neurogenesis and development through diverse neurological disorders. However, the cell-type specificity of brain miRs and tRFs remains poorly characterized, limiting the interpretation of their function. To address this issue, we generated a comprehensive, cell-type-resolved atlas of miRs and tRFs from live human brain tissues. Specifically, we isolated neurons, astrocytes, microglia, and oligodendrocytes from neurosurgery-obtained fresh human brain samples and profiled their miR and tRF repertoires using small RNA-sequencing. Our atlas revealed multiple differences in miR and tRF expression between the four cell types and consequently identified novel cell-type markers. Furthermore, we demonstrated that miR cell-type specificity may be regulated by quantitative trait loci located in cell-type-associated enhancer regions. We also report higher levels of 5'-tRNA halves in neurons compared to glia, including a particular neuronal enrichment of 5'-tRNA halves derived from glycine, leucine and lysine tRNAs. These neuronal tRFs were significantly upregulated in Alzheimer's disease postmortem brain samples compared to age-matched controls, possibly reflecting a neuronal response to disease. Our atlas, together with an accompanying statistical tool for miR cell-type enrichment analysis, provides a publicly available resource for delineating small RNA cell-type origin and function in the human brain.

Introduction

MicroRNAs (miRs) are short non-coding RNA molecules, typically up to 22 nucleotides long, that suppress gene expression through complementary binding to target mRNA transcripts[1,2]. Transfer RNA (tRNA) fragments (tRFs) are an additional species of short non-coding RNAs, 16-50 nucleotides long, that are generated by specific cleavage of a precursor or mature tRNA. They exert regulatory roles independently of their tRNA parent and can bind target mRNAs as well as interact directly with proteins[3]. miRs are well-established regulators of key brain processes[4,5], including neurodevelopment[6–11], synaptic plasticity[12–14], apoptosis[15,16], neuroinflammation[17], neurodegeneration[18,19], and epilepsy[5,20]. tRFs have

likewise been implicated in a growing number of neurological and neurodegenerative conditions[21,22], including Alzheimer's disease[23,24] (AD), Parkinson's disease[25] (PD), psychological stress[26], and neuronal ferroptosis[27]. However, despite extensive evidence for their involvement in brain function, the cell-type-specific expression of brain miRs and tRFs remains poorly characterized, limiting the functional interpretation of their regulatory roles.

While single-cell RNA sequencing (scRNA-seq) has revolutionized transcriptomics by enabling the study of gene regulation at the resolution level of the individual cell, small non-coding RNAs (sncRNAs) are rarely captured by scRNA-seq that measures only a fraction of the transcriptome, leaving many lowly expressed transcripts, including miRs, undetected[28]. Additionally, most scRNA-seq protocols rely on poly(T) priming to capture polyadenylated mRNAs, whereas most miRs and all tRFs are not polyadenylated[29]. Thus, most sncRNA studies still rely on bulk tissue samples that contain a variety of cell types. While several specialized protocols have been developed to measure miR expression at single-cell resolution, these approaches require dedicated methodology and are limited in the number of cells that can be profiled[30–34]. Currently, to the best of our knowledge, no human brain single-cell or cell-type-resolved miR datasets exist, that simultaneously include all major brain cell types. That being said, miRs do display cell-type-specific expression across multiple tissues[35,36], including the brain[32]. Similarly, brain tRNA expression patterns have been shown to vary between cell types[37], although cell-type-specific regulation of tRFs remains largely unexplored.

Here, we present the first cell-type-resolved atlas of miR and tRF expression patterns in live human brain, covering neurons, microglia, astrocytes and oligodendrocytes. To capture the transcriptome profiles of small RNAs in these populations, we collected brain tissue samples obtained during neurosurgical procedures, isolated single nuclei with a surrounding perinuclear cytoplasmic fraction[38], separated them to cell types by fluorescence-activated cell sorting (FACS), and performed small RNA sequencing on each fraction separately. This procedure enabled direct comparison of miR and tRF profiles across distinct brain cell populations, revealing both unique markers of individual cell types and shared transcripts co-expressed across cell types. We found that many cell-type-enriched miRs are associated with quantitative trait loci (miR-QTLs) located in the enhancer regions of the corresponding cell types, suggesting that miR-QTLs may contribute to the cell-type-associated differences in miR profiles. The tRFs also differed between cell types, with nuclear 5'-tRFs derived from glycine, lysine, and leucine tRNAs significantly elevated in neurons compared to both microglia and astrocytes. This tRF type was also elevated in postmortem prefrontal cortex samples from Alzheimer's disease (AD) patients as compared to controls, indicating that 5'-tRNA halves might reflect neuron-specific AD-associated pathology.

Our study provides a unique resource for investigating cell-type-specific expression patterns and functions of miRs and tRFs from live human brain. To further enhance the study of brain miRs at cell-type resolution, we introduce a statistical tool that employs our data to quantify the degree of cell-type-specific marker enrichment in a given set of miRs. Both the dataset and tool are available for interactive usage on our website (https://brain-visualization.vercel.app/).

Results

Simultaneous FACS sorting of neurons, astrocytes and microglia from live human brain tissue

To establish a cell-type-resolved resource of sncRNAs, we separated cell types by fluorescence-activated cell sorting (FACS), followed by small RNA sequencing of the sorted populations (Figure 1a). 39 live human brain samples (17 females, 22 males; ages 37–85; Table 1) were obtained during neurosurgeries for removal of non-infiltrative brain tumors, including meningiomas and metastases (Supplementary Table 1). We followed the NuNeX protocol[38], in which samples were fixed briefly with formalin and then dissociated into suspensions of single nuclei that retained a perinuclear cytoplasmic layer (Methods). Nuclei were stained with DAPI for the identification of single cells rather than debris or doublets (Figure 1b, c), and the preserved cytoplasmic fraction enabled the use of cytoplasmic markers to identify neurons (NeuN), astrocytes (GFAP) and microglia (IBA1).

Within the DAPI-positive population, manual gates for NeuN-, IBA1-, and GFAP-positive nuclei were defined using thresholds determined from non-stained controls of the same sample (Supplementary Figure 1a-f; Methods). To minimize overlap across populations, each sorting gate was refined in two stages by assessing its intersection with two other cell type populations (Figure 1b). In particular, NeuN (FITC) and IBA1 (Alexa 647) gates were first defined based on their overlap in the FITC vs the Alexa 647 space (Figure 1d) and then refined by excluding GFAP (Cy3)-positive events, yielding NeuN-clean and IBA1-clean populations (Figures 1e, f). Similarly, the initial GFAP (Cy3) gate was defined based on the overlap with the NeuN (FITC) signal (Figure 1e) and then refined by comparison to the IBA1 (Alexa 647)-associated signal (Figure 1f).

Total RNA was extracted from the sorted populations and used to validate their cell type identities by qPCR measurement of additional cell type markers. NeuN-positive nuclei expressed the neuronal markers SNAP25 and SYNPR (Figure 1g), GFAP-positive nuclei expressed the astrocytic markers AQP4 and ATP13A4 (Figure 1h), and IBA1-positive nuclei expressed the microglial markers ALOX5AP and CD74 (Figure 1i). No cell type expressed markers specific to any other cell type. Our gating strategy, combined with qPCR validation, enabled reliable assignment of neuronal, astrocytic and microglial identities to the FACS-sorted nuclei populations. Next, 66 samples with the highest RIN values were selected for small RNA-sequencing (24 NeuN-positive, 24 IBA1-positive, and 18 GFAP-positive; Table 1; Supplementary Table 1; Methods), yielding an atlas of cell-type-resolved miR and tRF profiles.

Table 1. Sample metadata

	Neurons (NEUN)	**Astrocytes (GFAP)**	**Microglia (IBA1)**	**Oligodendrocytes (OLIG2)**
Number of samples	24	18	24	14
Age (years)	62 ± 12 (37-75)	61 ± 14 (37-85)	60 ± 11 (41-75)	60 ± 13 (37-85)
Sex	8 females, 16 males	9 females, 9 males	10 females, 14 males	5 females, 9 males

Characterizing the cell-type-specificity of human brain miRs

We next leveraged our atlas to compare miR levels across brain cell types. To account for statistical dependencies in the data, such as repeated measurements from the same patient and global effects of batch, sex, age and pathology type, we used the dream framework[39]. This approach employs linear mixed-effects modeling to perform differential expression (DE) analysis while accommodating both fixed and random effects, such as cell type and patient ID, respectively. Variance partitioning revealed cell type as the strongest predictor of miR levels (mean explained variance 18.3%), followed by patient ID (mean explained variance 12%; Supplementary Figure 2a). By contrast, batch, pathology type, sex and age explained only minor fractions of variance (mean explained variances 3.0%, 0.7%, 0.5%, and 1.7%, respectively; Supplementary Figure 2a), highlighting the strong cell-type-specific regulation of miRs and validating that the tumor pathology had minimal influence on the miR profiles.

Furthermore, the miR profiles clustered according to their cell type label: k-means clustering resulted in sample division that closely matched the annotated cell types (Figure 2a and Supplementary Figure 2b), yielding a normalized mutual information (NMI) score of 0.8 (Methods). In contrast, the NMI score between the k-means clusters and batch labels was 0.1, implying that the miR profiles clustered by cell type rather than by batch (Figure 2a, Supplementary Figure 2c). To identify cell-type-enriched miRs we performed DE analysis in three pairwise comparisons (neurons vs. microglia, neurons vs. astrocytes and microglia vs. astrocytes), correcting for batch, pathology type, sex, age and patient ID (Figure 2b; Supplementary Tables 2-4). Out of 280 miRs expressed above a defined threshold (Methods), 209 were significantly differentially expressed (DE) in one of the pairwise cell type comparisons (Figure 2b). Specifically, we identified 191 DE miRs between neurons, and microglia,163 between neurons and astrocytes, 96 between microglia and astrocytes (Figure 2b).

To quantify overlaps between the DE miRs we performed three pairwise comparisons (Figure 2c): for each cell type we determined the miRs significantly elevated in comparison with the other two cell types. This yielded 82 miRs elevated in neurons, 115 in astrocytes, and 97 in microglia (Supplementary Table 5). Neurons and astrocytes featured elevated levels of 24 common miRs, compared to microglia; astrocytes and microglia featured elevated levels of 56 common miRs, compared to neurons, whereas neurons and microglia demonstrated increased levels of only 5 common miRs, compared to astrocytes (Supplementary table 5). After excluding these overlaps, we identified 53, 36, and 35 miRs uniquely enriched in neurons, microglia and astrocytes, respectively (Figure 2c).

The top miR markers for each cell type were defined as those with a log-fold change greater than 2 compared to both other cell types. We identified unique markers for each cell type: 23 in neurons,13 in microglia, and 6 in astrocytes (Figure 2d; Supplementary Table 5; Methods). For neurons, the top 5 (by fold change) included hsa-miR-935, hsa-129-2-3p, hsa-miR-7-5p and hsa-miR-137-3p, and hsa-miR-124-3p (Figure 2e). Their neuronal identities are well supported in the literature: miR-7 regulates neuronal death and glutamatergic signaling[40,41]; miR-137 is critical for neural development[42]; miR-935 and miR-129-2-3p are both elevated in epileptic brains and plasma[43]. Among astrocytic miRs, hsa-miR-92b-3p was enriched, and has previously been linked to astrocytes in murine brain[44] and shown to regulate glioblastoma development in human brain[45] (Figure 2f). Top microglial miRs included the hsa-miR-142 family, previously associated with microglia in murine brain[44] and linked to neuroinflammation in murine models[46,47] (Figure 2g).

MiRs that are enriched in two cell types but depleted in the third are of particular interest too, possibly pointing to shared cell-type functions (Supplementary Table 5). We found elevated levels of hsa-miR-9, a regulator of synaptic plasticity and memory[48], both in neurons and astrocytes (Supplementary Figure 2d). The hsa-miR-221/222 family, involved in neuroinflammation[49–51], was enriched both in neurons and microglia (Supplementary Figure 2e). Finally, glial miRs enriched in both microglia and astrocytes relative to neurons included hsa-miR-32-5p, linked to neuroinflammation mediated by both glial types[52,53] (Supplementary Figure 2f).

FACS isolation of oligodendrocytes derived from live human brain tissue

To enhance the depth of our cell-type-resolved atlas we also profiled sncRNAs from the fourth major brain cell type, oligodendrocytes. We used the well-established OLIG2 antibody, which requires an additional permeabilization step to allow antibody access to the nucleus. This necessitated separate staining and FACS sorting steps (Figure 3a; Methods). As in the original protocol (Figure 1), single cells were identified using DAPI (Supplementary Figure 3a), and OLIG2-positive nuclei were gated based on thresholds defined from non-stained controls (Supplementary Figure 3b, 3c; Methods). We profiled miRs and tRFs from 14 sorted OLIG2-positive populations (5 females, 9 males; Table 1), using small RNA sequencing.

Similarly to the other cell types, we used qPCR to measure enrichment of the oligodendrocyte biomarkers ENPP2 and MOBP in the OLIG2-positive fraction compared with neurons, microglia, and astrocytes, (Figure 3b). However, the OLIG2-positive population also featured increased levels of the neuronal marker SNAP25, the astrocyte markers AQP4 and ATP13A4 and the microglial marker ALOX5AP (Supplementary Figure 3d-f). Therefore, the OLIG2-positive group represents a mixed, albeit oligodendrocyte-enriched population.

The mixed identity of the OLIG2-positive population justified a different statistical approach to identify the oligodendrocyte-enriched miRs. We applied the dream framework[39] to identify oligodendrocyte-specific miRs by comparing the OlLIG2-positive population to the averaged profile of the three other cell types while correcting for batch, pathology type, sex, age and participant ID (Figure 3c; Supplementary Table 6; Methods). This analysis revealed 20 miRs that were significantly enriched in oligodendrocytes relative to all other cell types (Figures 3d). Notably, these included hsa-miR-219a and hsa-miR-338, both known to promote myelin repair[54], and hsa-miR-23, which enhances oligodendrocyte differentiation and myelin synthesis[55]. We also identified hsa-miR-181a-5p, previously implicated in oligodendrocyte maturation[56] and suggested as a potential epigenetic biomarker of multiple sclerosis[57]. To identify the oligodendrocyte miR markers we further excluded miRs with log-fold change lower than 2, as well as those that appeared as markers of other cell types, resulting in two miRs, uniquely enriched in the oligodendrocyte population: hsa-miR-181b-5p and hsa-miR-33b-5p (Figure 3e). The miR-33 family is associated with lipid metabolism in the brain[58], and the miR-181b family was implicated in myelin-assisted axon regeneration[59]. Altogether, we extracted the oligodendrocyte miR signature alongside neuron-, astrocyte-, and microglia-specific profiles, thereby extending our resource to encompass all four major brain cell types.

Cell-type-specific miRs are associated with cell-type-specific regulatory elements

Expression levels of miRs in the human brain were recently reported to be influenced by specific genetic variants, termed quantitative trait loci (miR-QTLs)[60]. We therefore hypothesized that cell-type-enriched miRs may be regulated by QTLs located within cell-type-specific promoter or enhancer regions (Figure 4a; Supplementary Table 7). Leveraging the previously annotated miR-QTLs[60], we identified 31 neuron-, 20 microglia-, 21 astrocyte-, and 4 oligodendrocyte-enriched miRs regulated by 152, 113, 108, and 39 QTLs, respectively. To examine whether these QTLs overlap with cell-type-specific regulatory regions we mapped their genomic coordinates to cell-type-specific promoter and enhancer annotations[61]. We then applied Fisher's exact test[62] to statistically evaluate the association between the cell-type-enriched miRs and their QTLs residing in cell-type-specific genomic regions. Neuronal miRs indeed showed a significant enrichment of QTLs within neuron-specific enhancers ($p = 2 \times 10^{-5}$; Figure 4b, left panel) and a similar, though weaker, enrichment trend was observed between astrocytic miRs and miR-QTLs residing in astrocyte-specific enhancer regions ($p = 0.0575$; Figure 4b, right panel). The association between microglial miRs and miR-QTLs in microglia-specific enhancers, as well as between oligodendrocyte-enriched miRs and miR-QTLs in oligodendrocyte-specific enhancers, did not reach statistical significance (Supplementary Figure 4b; Supplementary Table 7). Similarly, no significant associations were observed between miR levels and cell-type-specific promoter regions (Supplementary Table 7). These results collectively suggest that miR-QTLs residing in cell-type-specific enhancer regions may contribute to the genetic regulation of cell-type-specific miR expression.

We next investigated whether the genomic loci of cell-type-enriched miRs overlap with cell-type-specific cis-regulatory (CRE) regions[63] (Figure 4c). Using a single-cell chromatin accessibility atlas of the adult human brain[63] we mapped the genomic coordinates of cell-type-enriched miRs to chromatin regions differentially accessible in diverse cell types, and quantified their associations using Fisher's exact test (Methods). Microglial miRs showed the strongest association, being significantly enriched within microglia-specific CRE regions ($p = 0.0012$; Figure 4d; Supplementary Figure 4d, Supplementary Table 8), suggesting that chromatin accessibility contributes to the cell-type-specificity of microglial miRs.

Measuring cell-type enrichment in candidate miR sets

By revealing the cell-type-specific miR markers, our atlas can be used for deconvolution of cell-type-specific signals within a miR set of interest (Methods). Here, we provide a statistical framework that calculates the cell-type enrichment of a list of input miRs, such as a list of DE miRs from a bulk RNA-seq study. In detail, we calculate the fraction of each cell type's marker miRs present in the input list and assess the significance of the association using Fisher's exact test with multiple comparison correction[62] (Figure 5a). To maximize coverage, we include overlapping markers; thus, if an input miR is enriched in more than one cell type, it contributes to the enrichment of each type.

We applied this framework to a range of miR sets derived from small RNA-seq in studies of brain-related conditions and pathologies (Supplementary Table 9). The signature of 110 DE miRs identified in the AD study[64] showed significant enrichment for neuronal markers (Figure 5b). Similarly, 125 miRs altered in PD brains[65] were also enriched for neuronal markers (Figure 5c). This suggests that the miR signatures, associated with neurodegeneration, mainly reflect neuronal processes. In contrast, the 63 miRs associated with multiple sclerosis[66] (MS) were predominantly enriched in oligodendrocyte-specific miRs, but also showed significant contributions of astrocyte and microglia markers, consistent with the role of glial-driven neuroinflammation in MS[67] (Figure 5d). A curated set of 17 miRs functionally linked to oligodendrocyte differentiation was enriched for the oligodendrocyte and astrocyte signatures, further validating our framework[68] (Figure 5e). We also examined a murine aging-related miR study comprising 476 miRs[69], and although this set contained markers from all major brain cell types, only microglial

enrichment was statistically significant, consistent with the original study that highlighted microglial miR involvement in brain aging[69] (Figure 5f). In summary, our cell-type-resolved brain miR atlas enabled the assignment of miR signatures to specific brain cell types, providing a powerful tool for interpreting bulk miR profiling studies.

Cell-type specificity of tRFs

Transfer RNA fragments are a recently re-identified family of sncRNAs, and have been implicated in various neurological conditions[21,22]. Once considered to be inert degradation products of tRNAs, tRFs are now recognized as independent regulators that act either by interacting with target RNAs, in a manner similar to that of microRNAs[26,70,71], or by directly binding proteins[27,72]. Using our cell-type-resolved sncRNA atlas, we were able to characterize the cell-type specificity of brain expression profiles of tRFs, in addition to those of miRs.

tRFs exhibit strong sequence similarity: fragments derived from the same tRNA share most of their sequence, and even those originating from different tRNAs exhibit similarity due to high conservation in the tRNA genes themselves[73]. We therefore analyzed tRFs at the level of families, defined by genome of origin (nuclear or mitochondrial), amino acid identity of the parent tRNA, and cleavage type[26] (Figure 6a). Collapsing raw tRF counts into family sums reduced noise and increased the variance explained by the cell type factor (Supplementary Figure 5a, b). However, unlike miR profiles, tRFs expression profiles displayed a stronger batch effect, requiring more rigorous correction with ComBat-seq[74] (Supplementary Figure 5b; Methods).

To determine the cell-type specificity of each tRF family, we conducted pairwise DE analyses between three cell type pairs (neurons vs. astrocytes, neurons vs. microglia, and astrocytes vs. microglia) using the Mann–Whitney non-parametric test after batch correction. Neurons exhibited the most distinct tRF profiles (Figure 6b), with 14 enriched tRF families (Figure 6c, 6d, 6e) compared to 4 in microglia (Figure 6c) and none in astrocytes (Figure 6d), resulting in 18 cell-type-enriched families (Figure 6e, Supplementary table 10). Ten out of 14 tRF families elevated in neurons represented the 5’ half of their tRNA of origin (5’-halves or 5’-tRFs; Figure 6c, 6d, 6e). By contrast, all 4 microglia-enriched families were derived from the 3’ halves of mitochondrial tRNAs (Figure 6c, 6d, 6e). Overall, tRF profiles showed a weaker cell type effect than miRs, with an NMI of 0.04 between k-means clusters and cell type labels, compared to 0.8 for miRs (Supplementary Figure 5c).

We next compared the mean tRF family levels for each cleavage type, identifying a significant elevation of 5’-tRF and 5’-half families in neurons compared to both microglia and astrocytes (Figure 6f). Specifically, the Nuc-Gly-5′-half, Nuc-Leu-5′-half, and Nuc-Lys-5′-half families were significantly upregulated in neurons relative to both astrocytes and microglia (Figure 6g), highlighting them as candidates for neuron-specific tRF markers.

Comparison of tRF family profiles between the oligodendrocyte-enriched population and other cell types identified four significantly enriched families; however, the effect sizes were small (Supplementary Table 11; Supplementary Figure 5d). Notably, the tRF families with the highest log fold change were derived from mitochondrial tRNAs, potentially reflecting differences in the oligodendrocyte isolation protocol, which required a nucleus permeabilization step (Methods).

To determine if we could identify cell-type-specific signals in bulk tRF profiles, we re-aligned a small RNA dataset of postmortem prefrontal cortex (PFC) samples from AD patients and age-matched controls (n=6 each group)[75] to the tRF reference database[76]. We performed DE analysis using DESeq2[77] (Figure 6h). Remarkably, nuclear 5'-derived tRNA halves, enriched in neurons in our atlas, were consistently upregulated in AD, with 72% of expressed 5'-tRNA-halves significantly elevated in AD (Figure 6h; Supplementary Table 12). In particular, the neuron-enriched Nuc-Gly-5'-halves, Nuc-Leu-5'-halves and Nuc-Lys-5'-halves were also upregulated, potentially reflecting a neuron-specific process linked to AD pathology (Figure 6i).

Discussion

In this study we have established the first cell-type-resolved atlas of miR and tRF expression profiles in live human brain. By identifying both unique and shared miR markers across four major brain cell types we show that the brain miR profiles are highly cell-type-specific. Furthermore, we propose that miR cell-type specificity may be regulated by miR-QTLs and by miR genes residing within cell-type-associated genomic regions such as cell-type-specific enhancers and other cis-regulatory elements.

We have also introduced a statistical framework for cell-type enrichment analysis of miR lists of interest. Since no robust, commercial scRNA-seq technology currently enables the capture of small RNA profiles, most studies of brain small RNAs are based on bulk RNA-seq. In this context, our atlas offers an opportunity to deconvolve cell-type signals from bulk-derived miR profiles. Once scalable single-cell small RNA sequencing becomes feasible, our resource may also serve as a reference resource for cell type annotation, providing validated miR markers for neuronal and glial populations.

While miRs are encoded by their own genes, tRFs are generated by the cleavage of tRNAs, ubiquitous and essential to all cells for survival. It is therefore biologically reasonable that tRFs exhibit a less pronounced cell-type effect than miRs. Nevertheless, we found that neurons exhibit distinct tRF signatures compared to both astrocytes and microglia, which could be explained by cell-type-specific tRF production or degradation rates that are affected by differential expression of the corresponding ribonucleases. Neurons are particularly enriched in nuclear tRF families aligned to the 5' side of their tRNAs of origin, and we identified three distinct tRF families as candidate markers: Nuc-Gly-5'-half, Nuc-Leu-5'-half and Nuc-Lys-5'-half. Moreover, these families are also robustly elevated in AD, suggesting that they may reflect a neuron-specific response to AD pathology. Interestingly, Nuc-Lys-5'-half was recently reported to regulate neuronal ferroptosis in the context of botulinum intoxication[27].

Our atlas was generated from fresh human brain tissue, which, on the one hand, represents its unique strength by avoiding postmortem transcriptional artifacts. On the other hand, a potential limitation of our study is the possible influence of tumor-related processes on the small RNA profiles. To minimize this effect, we obtained specimens only during resections of non-invasive brain tumors. All the tumors resected were non-infiltrative and external to the brain, originating from the meninges in meningioma or from non-neural tissue in metastases. Accordingly, our previous work on this cohort[78] demonstrated that these samples are transcriptionally closer to postmortem human brain tissues than to tumor-associated profiles, suggesting minimal contamination. Additionally, our statistical analysis demonstrated minimal effect of the tumor pathology on both miR and tRF profiles.

In summary, this study represents a significant step toward deciphering the small RNA landscape of human brain cells. Future work could extend this atlas to finer cellular states such as neuronal subtypes

or disease-associated glial populations[79–81], and integrate emerging single-cell small-RNA sequencing technologies to achieve higher resolution. Both our cell-type-resolved miR and tRF atlases, and the miR cell-type deconvolution tool are publicly available for interactive exploration on our portal (https://brain-visualization.vercel.app/).

Methods

Tissue samples

The study, including acquisition of cortical brain samples, was approved by the Rambam Medical Center institutional review board and by the national ethical review board (IRB protocol RMB-0713-19). All patients signed informed consent forms. Biopsies were extracted during resection operations of non-neural pathologies such as meningiomas and metastases, with exclusion of patients who were operated on for neural pathologies (e.g., gliomas). Tissue samples were fixed in 4% formaldehyde (Sigma-Aldrich, HT501128) for 30 minutes, washed with PBS (Merck, D8537) and stored at 4°C in RNA*later*® (Merck, R0901) for 1-3 days until homogenization.

NuNeX

Brain sections (average size of 3 x 5 mm) were homogenized in 5 mL nuclear isolation buffer (10mM Tris pH 8.0, 25 mM KCl, 5 mM $MgCl_2$, 0.1% Triton, 250 mM sucrose, 1 mM DTT) containing RNase inhibitor (1:100, NEB, M0314) and Protease Inhibitor Cocktail (1:00, Cell Signaling Technology, 5871), using a Dounce tissue grinder (Sigma-Aldrich, D9063). The homogenate was passed through a 40 µm cell strainer (Corning, 352340) and pelleted by centrifugation at 900 *g* for 5 min. Cells (nuclei with attached perinuclear cytoplasm) were resuspended in 1 mL staining buffer (PBS containing 0.8% BSA, RNase Inhibitor as above) and stored in Eppendorf test tubes at -80°C until FACS sorting.

Immunostaining of neurons, astrocytes, and microglia

Samples were incubated for 20 minutes in 20 µL of Fc block (Invitrogen,14-9161-73) in staining buffer. Primary antibodies were then added for 30 minutes as follows: labelled anti-NeuN for neurons (1:500; Alexa Fluor™488 conjugated, Merck, MAB377X), anti-GFAP for astrocytes (1:1000; Invitrogen, 14-9892-80), and anti-Iba1 for microglia (1:500; Abcam, ab178846). Cells were pelleted by centrifugation at 900 *g* for 5 minutes, resuspended in staining buffer, and incubated for 30 minutes with secondary antibodies for neurons (1:500; Alexa Fluor™ 647 conjugated, Jackson ImmunoResearch, 711-605-152) and astrocytes (1:500; Cy3-conjugated; Jackson ImmunoResearch, 115-165-072). Cells were pelleted again as above and resuspended in staining buffer containing DAPI (1µg/mL; Santa Cruz, sc-3598). All steps were performed on ice or at 4°C.

Immunostaining of oligodendrocytes

For oligodendrocyte isolation, nuclei were fixated and permeabilized using a specialized kit (Invitrogen, 00-5523-00), according to the manufacturer's protocol. Anti-OLIG2 (1:100; Invitrogen, P21954) was then added in staining buffer (PBS, 0.8% BSA, RNase Inhibitor) for 1 hour. Following centrifugation and resuspension in staining buffer cells were incubated with a secondary antibody (1:200; Alexa Fluor™ 647 conjugated, Jackson ImmunoResearch, 711-605-152) for 30 minutes. Cells were pelleted again as above and resuspended in staining buffer containing DAPI (1µg/mL; Santa Cruz, sc-3598). All steps were performed on ice or at 4°C.

FACS-sorting

NeuN-, GFAP-, Iba1-, and OLIG2-positive cells were sorted through a 85 µm nozzle with an approximate flow rate of 8,000 events/s. Sorted populations (> 1,000 cells) were collected into tubes containing 500 µL

staining buffer. Sample collection was done with BD FACSAria III (BD Biosciences) and analysis with FCS Express 7 Software (*De Novo* Software).

RNA extraction

Cells were centrifuged at 900 *g* for 5 minutes, resuspended in 100 µL PKD buffer (RNeasy FFPE Kit, Qiagen, 73504) and RNA was extracted (RNeasy FFPE Kit) according to manufacturer's instructions. Concentration and RIN were determined (Bioanalyzer 6000, Agilent Technologies), with concentrations between 0.1-12.1 ng/µL and RIN between 1.2 and 7.4. The RIN range most likely reflects varying amounts of rRNA present in the samples, in addition to possible cleavage due to the formaldehyde fixation, and not low RNA quality due to degradation.

RT-qPCR

Synthesis of cDNA from lncRNA and mRNA was done using qScript™ cDNA Synthesis Kit (Quantabio, 95047) and qPCR was done using PerfeCTa® SYBR® Green FastMix® (Quantabio, 95072) with human-specific forward and reverse primers (Supplementary Table 13). The CFX384 Touch Real-Time PCR System (Bio-Rad) was used for quantification and the CFX Maestro software (Bio-Rad v4.1.2433.1219) for extracting Cq values. The reference genes were β-actin and GAPDH. All primers were human-specific.

RNA sequencing and alignment

Libraries for short RNA sequencing were constructed in two batches from 500 pg (Batch 1) and 1000 pg (Batch 2) total RNA, using the D-Plex Small RNA-seq Kit for Illumina (Diagenode, C05030001) and Single Indexes for Illumina - Set #B (Diagenode, C05030011). The small RNA fraction was separated (Invitrogen, G401004) and verified (TapeStation, Agilent Technologies), then sequenced (Illumina, 20046810 or 20046811) using the NextSeq 2000 System (Illumina) at the Center for Genomic Technologies, the Hebrew University of Jerusalem. Small RNA was aligned to miRBase 22.1 (Kozomara et al, 2019; Griffiths-Jones et al, 2007) using miRDeep (Friedländer et al, 2008) and to the tRNA transcriptome using MINTmap (Loher et al, 2017) to MINTbase v2.0 (Pliatsika et al, 2016).

MicroRNA DE analysis

Raw read counts were preprocessed using DESeq2 (Love et al., 2014). Library size normalization factors were estimated using the estimateSizeFactors function to correct for sequencing depth across samples. Lowly expressed genes were filtered out by requiring counts per million (CPM) > 1 in at least 50% of samples. For the retained genes, normalized expression values were transformed as $\log_2(\text{CPM} + 1)$.
To quantify the contribution of biological and technical factors to expression variability we used the variancePartition framework (Hoffman & Schadt, 2016). Variance components were estimated using the linear mixed model with the formula $\sim(1|ID) + (1|Sex) + (1|Batch) + (1|Cell.type) + Age$, allowing estimation of the proportion of variance explained by donor identity, sex, batch, cell type, and age.
DE analysis was then performed using the dream framework implemented in variancePartition, which models both fixed and random effects. The DE model was defined as $\sim 0 + Cell.Type + Batch + Sex + Age + (1|ID)$. Pairwise contrasts were computed to compare Neurons vs Microglia, Microglia vs Astrocytes, and Neurons vs Astrocytes. To identify oligodendrocyte-enriched fragments a specific contrast comparing oligodendrocytes against all other cell types combined was constructed using the same model formulation: $Cell.typeOligodendrocytes - \frac{1}{3}(Cell.typeNeurons + Cell.typeMicroglia + Cell.typeAstrocytes)$. Model fitting was performed with dream (Hoffman & Roussos, 2021) and limma's eBayes functions (Ritchie et al, 2015).

MiR mapping to cell-type-specific miR-QTLs and CREs
Annotated miR-QTLs were derived (Vattathil et al, 2025) and the cell-type-specific enhancer and promoter region annotation were determined (Nott et al, 2019). To map miR genes to cell-type-specific CREs we retrieved the genomic coordinates of all annotated miRs from miRbase 22.1 (Kozomara et al, 2019; Griffiths-Jones et al, 2007). For each miR we then extracted its chromosomal position and extended the genomic interval by 500 bases upstream and downstream, to account for minor positional uncertainty and local regulatory proximity. Each extended miR interval was then intersected with the set of open chromatin regions defined as candidate CREs (Li et al., 2023). Four major brain cell classes (neurons, astrocytes, microglia, and oligodendrocytes) were defined based on the provided cell type hierarchical taxonomy (Li et al, 2023) and all corresponding fine-grained cell types were grouped under these classes.

Cell type signal deconvolution
To infer the cellular enrichment of bulk-derived miR lists we implemented a reference-based deconvolution approach based on our cell-type-specific atlas. This was done by computing the overlap between the input miR list and the lists of cell-type specific markers and calculating the fraction of cell-type-specific marker miRs detected in the input. To statistically assess whether an observed overlap exceeded random expectation we applied Fisher's exact test. For each cell type, a 2 × 2 contingency table was constructed representing: (i) the number of overlapping miRs between the input and the cell type markers, (ii) the number of miRs present in the input but not among that cell type markers, (iii) the number of miRs specific to the cell type but absent from the input, and (iv) the remaining background miRs not belonging to either set. One-sided Fisher's exact tests (alternative = 'greater') were used to identify significant cell type enrichments. Resulting *p*-values were corrected for multiple testing using the false discovery rate (FDR) method, yielding adjusted *p*-values.

tRF statistical analysis
The tRFs were divided into families defined by genome origin (nuclear/mitochondrial), associated amino acid, side (5' or 3') of the tRNA of origin to which the tRF was aligned, and cleavage type (tRNA half, cleaved at the anticodon loop, or tRF, cleaved elsewhere). The counts of all single tRFs in each family were summed. Batch correction was performed using pyComBat (Behdenna et al, 2023). Pairwise statistical comparisons were performed between each pair of the three cell types (neurons, astrocytes, and microglia) using the non-parametric Mann–Whitney U test. The resulting *p*-values were adjusted for multiple comparisons using the Benjamini–Hochberg FDR correction ($\alpha = 0.05$). Comparisons with adjusted $p < 0.05$ were considered statistically significant.

Comparing tRF profiles between AD and control brain samples
Raw fastq files from short RNA-Seq of Alzheimer's disease subjects and controls were downloaded from the GEO database (accession number GSE48552) and aligned to the tRNA transcriptome using MINTmap (Loher et al, 2017) to MINTbase v2.0 (Pliatsika et al, 2016). DE analysis was performed using the DESeq2 package (Love et al, 2014) on tRFs with median expression above 10 counts per million (CPM).

Data availability

Raw and processed data generated in this study are available in GEO under accession number GSE314790. In addition, both the atlas and the miR cell-type deconvolution framework are available on our website for interactive exploration (https://brain-visualization.vercel.app/).

Acknowledgements

We would like to thank the neurosurgery patients who contributed to this study. We would also like to express our gratitude to Dr. Nadav Yayon, a former PhD student in the lab (currently at the Cambridge Stem Cell Institute) for developing NuNeX and for assisting with the experimental pipeline; to Dr. Ola Karmi from the Research Infrastructures Unit of the Hebrew University of Jerusalem, Edmond J. Safra Campus - Givat Ram, for her guidance and assistance in FACS sorting; and to all members of the Soreq lab for assistance and constructive input. This work was supported by the Israel Science Foundation (ISF 835/23 to H. S.), Keter Holdings, Ken Stein and William Kilberg foundations (to H.S.) and a joint grant from the Shaare Zedek Medical Center, Jerusalem (to I. P. and H. S.). Serafima Dubnov is an awardee of PhD fellowships from the Azrieli, Kaete Klausner and Teva Foundations.

Declaration of generative AI and AI-assisted technologies in the manuscript preparation process

During the preparation of this work the authors used ChatGPT (version 5.2) to improve the grammar and syntax of the manuscript. After using this tool/service, the authors reviewed and edited the content as needed and take full responsibility for the content of the published article.

Declaration of interests

The authors declare no competing interests.

References

1. Gebert, L. F. R. & MacRae, I. J. Regulation of microRNA function in animals. *Nat Rev Mol Cell Biol* **20**, 21–37 (2019).
2. Kosik, K. S. MicroRNAs and Cellular Phenotypy. *Cell* **143**, 21–26 (2010).
3. Magee, R. & Rigoutsos, I. On the expanding roles of tRNA fragments in modulating cell behavior. *Nucleic Acids Research* **48**, 9433–9448 (2020).
4. Kosik, K. S. The neuronal microRNA system. *Nat Rev Neurosci* **7**, 911–920 (2006).
5. Brennan, G. P. & Henshall, D. C. MicroRNAs as regulators of brain function and targets for treatment of epilepsy. *Nat Rev Neurol* **16**, 506–519 (2020).
6. Pearson, J. C., Lemons, D. & McGinnis, W. Modulating Hox gene functions during animal body patterning. *Nat Rev Genet* **6**, 893–904 (2005).
7. Giraldez, A. J. *et al.* MicroRNAs Regulate Brain Morphogenesis in Zebrafish. *Science* **308**, 833–838 (2005).

8. Wienholds, E. *et al.* MicroRNA Expression in Zebrafish Embryonic Development. *Science* **309**, 310–311 (2005).
9. Krichevsky, A. M., Sonntag, K.-C., Isacson, O. & Kosik, K. S. Specific MicroRNAs Modulate Embryonic Stem Cell–Derived Neurogenesis. *Stem Cells* **24**, 857–864 (2006).
10. Xu, B., Karayiorgou, M. & Gogos, J. A. MicroRNAs in psychiatric and neurodevelopmental disorders. *Brain Research* **1338**, 78–88 (2010).
11. Gu, X. *et al.* Molecular Mechanisms Involved in the Regulation of Neurodevelopment by miR-124. *Mol Neurobiol* **60**, 3569–3583 (2023).
12. Bredy, T. W., Lin, Q., Wei, W., Baker-Andresen, D. & Mattick, J. S. MicroRNA regulation of neural plasticity and memory. *Neurobiology of Learning and Memory* **96**, 89–94 (2011).
13. Cohen, J. E., Lee, P. R., Chen, S., Li, W. & Fields, R. D. MicroRNA regulation of homeostatic synaptic plasticity. *Proc. Natl. Acad. Sci. U.S.A.* **108**, 11650–11655 (2011).
14. Portugal, R. *et al.* Shaping the synapse through neuronal activity-regulated miRNAs. *Trends in Neurosciences* **48**, 679–690 (2025).
15. Chan, J. A., Krichevsky, A. M. & Kosik, K. S. MicroRNA-21 Is an Antiapoptotic Factor in Human Glioblastoma Cells. *Cancer Research* **65**, 6029–6033 (2005).
16. Beylerli, O., Gareev, I., Sufianov, A., Ilyasova, T. & Zhang, F. The role of microRNA in the pathogenesis of glial brain tumors. *Non-coding RNA Research* **7**, 71–76 (2022).
17. Zhang, J., Li, A., Gu, R., Tong, Y. & Cheng, J. Role and regulatory mechanism of microRNA mediated neuroinflammation in neuronal system diseases. *Front. Immunol.* **14**, 1238930 (2023).
18. Hébert, S. S. & De Strooper, B. Alterations of the microRNA network cause neurodegenerative disease. *Trends in Neurosciences* **32**, 199–206 (2009).
19. Li, Y.-B. *et al.* MicroRNAs: pioneering regulators in Alzheimer's disease pathogenesis, diagnosis, and therapy. *Transl Psychiatry* **14**, 367 (2024).
20. Sonawane, S., Všianský, V. & Brázdil, M. MicroRNA-mediated regulation of neurotransmitter receptors in epilepsy: A systematic review. *Epilepsy & Behavior* **158**, 109912 (2024).
21. Winek, K. & Soreq, H. Emerging roles of transfer RNA fragments in the CNS. *Brain* **148**, 2631–2645 (2025).

22. Dubnov, S. & Soreq, H. Transfer RNA Fragments, from Structure to Function. in *RNA Structure and Function* (ed. Barciszewski, J.) vol. 14 1–19 (Springer International Publishing, Cham, 2023).
23. Shulman, D. *et al.* Sex-specific declines in cholinergic-targeting tRNA fragments in the nucleus accumbens in Alzheimer's disease. *Alzheimer's & Dementia* alz.13095 (2023) doi:10.1002/alz.13095.
24. Wu, W., Lee, I., Spratt, H., Fang, X. & Bao, X. tRNA-Derived Fragments in Alzheimer's Disease: Implications for New Disease Biomarkers and Neuropathological Mechanisms. *JAD* **79**, 793–806 (2021).
25. Madrer, N. *et al.* Pre-symptomatic Parkinson's disease blood test quantifying repetitive sequence motifs in transfer RNA fragments. *Nat Aging* **5**, 868–882 (2025).
26. Vaknine Treidel, S. *et al.* Maternal prenatal stress induces sex-dependent changes in tRNA fragment families and cholinergic pathways in newborns. *Mol Psychiatry* **30**, 4307–4319 (2025).
27. Monash, A. *et al.* 5′LysTTT tRNA fragments support survival of botulinum-intoxicated neurons by blocking ferroptosis. *Genomic Psychiatry* 1–17 (2025) doi:10.61373/gp025a.0047.
28. AlJanahi, A. A., Danielsen, M. & Dunbar, C. E. An Introduction to the Analysis of Single-Cell RNA-Sequencing Data. *Molecular Therapy - Methods & Clinical Development* **10**, 189–196 (2018).
29. Kolodziejczyk, A. A., Kim, J. K., Svensson, V., Marioni, J. C. & Teichmann, S. A. The Technology and Biology of Single-Cell RNA Sequencing. *Molecular Cell* **58**, 610–620 (2015).
30. Faridani, O. R. *et al.* Single-cell sequencing of the small-RNA transcriptome. *Nat Biotechnol* **34**, 1264–1266 (2016).
31. Hagemann-Jensen, M., Abdullayev, I., Sandberg, R. & Faridani, O. R. Small-seq for single-cell small-RNA sequencing. *Nat Protoc* **13**, 2407–2424 (2018).
32. Nowakowski, T. J. *et al.* Regulation of cell-type-specific transcriptomes by microRNA networks during human brain development. *Nat Neurosci* **21**, 1784–1792 (2018).
33. Li, J., Zhang, Z., Zhuang, Y., Wang, F. & Cai, T. Small RNA transcriptome analysis using parallel single-cell small RNA sequencing. *Sci Rep* **13**, 7501 (2023).
34. Wang, N. *et al.* Single-cell microRNA-mRNA co-sequencing reveals non-genetic heterogeneity and mechanisms of microRNA regulation. *Nat Commun* **10**, 95 (2019).

35. Liu, B. *et al.* Cell type–specific microRNA therapies for myocardial infarction. *Sci. Transl. Med.* **13**, eabd0914 (2021).
36. Monticelli, S. *et al.* MicroRNA profiling of the murine hematopoietic system. *Genome Biol* **6**, R71 (2005).
37. Kapur, M., Molumby, M. J., Guzman, C., Heinz, S. & Ackerman, S. L. Cell-type-specific expression of tRNAs in the brain regulates cellular homeostasis. *Neuron* **112**, 1397-1415.e6 (2024).
38. Yayon, N. *et al.* High-throughput morphometric and transcriptomic profiling uncovers composition of naïve and sensory-deprived cortical cholinergic VIP/CHAT neurons. *The EMBO Journal* **42**, e110565 (2023).
39. Hoffman, G. E. & Roussos, P. Dream: powerful differential expression analysis for repeated measures designs. *Bioinformatics* **37**, 192–201 (2021).
40. Cerda-Jara, C. A. *et al.* miR-7 controls glutamatergic transmission and neuronal connectivity in a Cdr1as-dependent manner. *EMBO Rep* **25**, 3008–3039 (2024).
41. Scoyni, F. *et al.* ciRS-7 and miR-7 regulate ischemia-induced neuronal death via glutamatergic signaling. *Cell Reports* **43**, 113862 (2024).
42. Mahmoudi, E. & Cairns, M. J. MiR-137: an important player in neural development and neoplastic transformation. *Mol Psychiatry* **22**, 44–55 (2017).
43. Sun, Y. *et al.* Expression of microRNA-129-2-3p and microRNA-935 in plasma and brain tissue of human refractory epilepsy. *Epilepsy Research* **127**, 276–283 (2016).
44. Isakova, A., Fehlmann, T., Keller, A. & Quake, S. R. A mouse tissue atlas of small noncoding RNA. *Proc. Natl. Acad. Sci. U.S.A.* **117**, 25634–25645 (2020).
45. Grafals-Ruiz, N. *et al.* MicroRNA-92b targets tumor suppressor gene FBXW7 in glioblastoma. *Front. Oncol.* **13**, (2023).
46. Roblain, Q. *et al.* Intravitreal injection of anti-miRs against miR-142-3p reduces angiogenesis and microglia activation in a mouse model of laser-induced choroidal neovascularization. *Aging* **13**, 12359–12377 (2021).
47. Gupta, N. *et al.* miR-142-3p Regulates BDNF Expression in Activated Rodent Microglia Through Its Target CAMK2A. *Front. Cell. Neurosci.* **14**, 132 (2020).

48. Sim, S.-E. *et al.* The Brain-Enriched MicroRNA miR-9-3p Regulates Synaptic Plasticity and Memory. *J. Neurosci.* **36**, 8641–8652 (2016).

49. Shan, Y., Hu, J., Lv, H., Cui, X. & Di, W. miR-221 Exerts Neuroprotective Effects in Ischemic Stroke by Inhibiting the Proinflammatory Response. *Journal of Stroke and Cerebrovascular Diseases* **30**, 105489 (2021).

50. Liang, T., Liu, Y., Liu, R., Shen, X. & Xu, M. miR-221 activates Sox11 to reduce brain injury after intracerebral hemorrhage via inhibiting neuroinflammation. *Sci Rep* **15**, 29643 (2025).

51. Bai, Y. & Niu, J. miR-222 regulates brain injury and inflammation following intracerebral hemorrhage by targeting ITGB8. *Mol Med Report* https://doi.org/10.3892/mmr.2019.10903 (2019) doi:10.3892/mmr.2019.10903.

52. Yan, T. *et al.* miR-32-5p-mediated Dusp5 downregulation contributes to neuropathic pain. *Biochemical and Biophysical Research Communications* **495**, 506–511 (2018).

53. Zhong, X. *et al.* MicroRNA-32-5p knockout eliminates lipopolysaccharide-induced depressive-like behavior in mice through inhibition of astrocyte overactivity. *Brain, Behavior, and Immunity* **84**, 10–22 (2020).

54. Wang, H. *et al.* miR-219 Cooperates with miR-338 in Myelination and Promotes Myelin Repair in the CNS. *Developmental Cell* **40**, 566-582.e5 (2017).

55. Lin, S.-T. *et al.* MicroRNA-23a promotes myelination in the central nervous system. *Proc. Natl. Acad. Sci. U.S.A.* **110**, 17468–17473 (2013).

56. Letzen, B. S. *et al.* MicroRNA Expression Profiling of Oligodendrocyte Differentiation from Human Embryonic Stem Cells. *PLoS ONE* **5**, e10480 (2010).

57. Edgünlü, T. G. *et al.* miR-181a-5p is a potential candidate epigenetic biomarker in multiple sclerosis. *Genome* **65**, 547–561 (2022).

58. Jaouen, F. & Gascon, E. Understanding the Role of miR-33 in Brain Lipid Metabolism: Implications for Alzheimer's Disease. *J. Neurosci.* **36**, 2558–2560 (2016).

59. Deng, B. *et al.* Electroacupuncture enhances rehabilitation through miR-181b targeting PirB after ischemic stroke. *Sci Rep* **6**, 38997 (2016).

60. Vattathil, S. M. *et al.* Mapping the microRNA landscape in the older adult brain and its genetic contribution to neuropsychiatric conditions. *Nat Aging* **5**, 306–319 (2024).

61. Nott, A. *et al.* Brain cell type–specific enhancer–promoter interactome maps and disease **-** risk association. *Science* **366**, 1134–1139 (2019).

62. Fisher, R. A. On the Interpretation of χ 2 from Contingency Tables, and the Calculation of P. *Journal of the Royal Statistical Society* **85**, 87 (1922).

63. Li, Y. E. *et al.* A comparative atlas of single-cell chromatin accessibility in the human brain. *Science* **382**, eadf7044 (2023).

64. Luo, T. *et al.* Brain microRNAs differentially expressed in age-related cerebral pathologies. *Neurobiology of Aging* **151**, 42–53 (2025).

65. Hoss, A. G., Labadorf, A., Beach, T. G., Latourelle, J. C. & Myers, R. H. microRNA Profiles in Parkinson's Disease Prefrontal Cortex. *Front. Aging Neurosci.* **8**, (2016).

66. Junker, A., Hohlfeld, R. & Meinl, E. The emerging role of microRNAs in multiple sclerosis. *Nat Rev Neurol* **7**, 56–59 (2011).

67. Absinta, M. *et al.* A lymphocyte–microglia–astrocyte axis in chronic active multiple sclerosis. *Nature* **597**, 709–714 (2021).

68. Zhao, X. *et al.* MicroRNA-Mediated Control of Oligodendrocyte Differentiation. *Neuron* **65**, 612–626 (2010).

69. Engel, A. *et al.* A spatio-temporal brain miRNA expression atlas identifies sex-independent age-related microglial driven miR-155-5p increase. *Nat Commun* **16**, (2025).

70. Schopman, N. C. T., Heynen, S., Haasnoot, J. & Berkhout, B. A miRNA-tRNA mix-up: tRNA origin of proposed miRNA. *RNA Biology* **7**, 573–576 (2010).

71. Winek, K. *et al.* Transfer RNA fragments replace microRNA regulators of the cholinergic poststroke immune blockade. *Proc. Natl. Acad. Sci. U.S.A.* **117**, 32606–32616 (2020).

72. Tzur, Y. *et al.* Lysine tRNA fragments and miR-194-5p co-regulate hepatic steatosis via β-Klotho and perilipin 2. *Molecular Metabolism* **79**, 101856 (2024).

73. Giegé, R. *et al.* Structure of transfer RNAs: similarity and variability. *WIREs RNA* **3**, 37–61 (2012).

74. Zhang, Y., Parmigiani, G. & Johnson, W. E. ComBat-seq: batch effect adjustment for RNA-seq count data. *NAR Genomics and Bioinformatics* **2**, lqaa078 (2020).

75. Lau, P. *et al.* Alteration of the micro RNA network during the progression of Alzheimer's disease. *EMBO Mol Med* **5**, 1613–1634 (2013).

76. Loher, P., Telonis, A. G. & Rigoutsos, I. MINTmap: fast and exhaustive profiling of nuclear and mitochondrial tRNA fragments from short RNA-seq data. *Sci Rep* **7**, 41184 (2017).

77. Love, M. I., Huber, W. & Anders, S. Moderated estimation of fold change and dispersion for RNA-seq data with DESeq2. *Genome Biol* **15**, 550 (2014).

78. Dubnov, S. *et al.* Knockout of the longevity gene Klotho perturbs aging and Alzheimer's disease-linked brain microRNAs and tRNA fragments. *Commun Biol* **7**, 720 (2024).

79. Habib, N. *et al.* Disease-associated astrocytes in Alzheimer's disease and aging. *Nat Neurosci* **23**, 701–706 (2020).

80. Deczkowska, A. *et al.* Disease-Associated Microglia: A Universal Immune Sensor of Neurodegeneration. *Cell* **173**, 1073–1081 (2018).

81. Kenigsbuch, M. *et al.* A shared disease-associated oligodendrocyte signature among multiple CNS pathologies. *Nat Neurosci* **25**, 876–886 (2022).

Figure 1

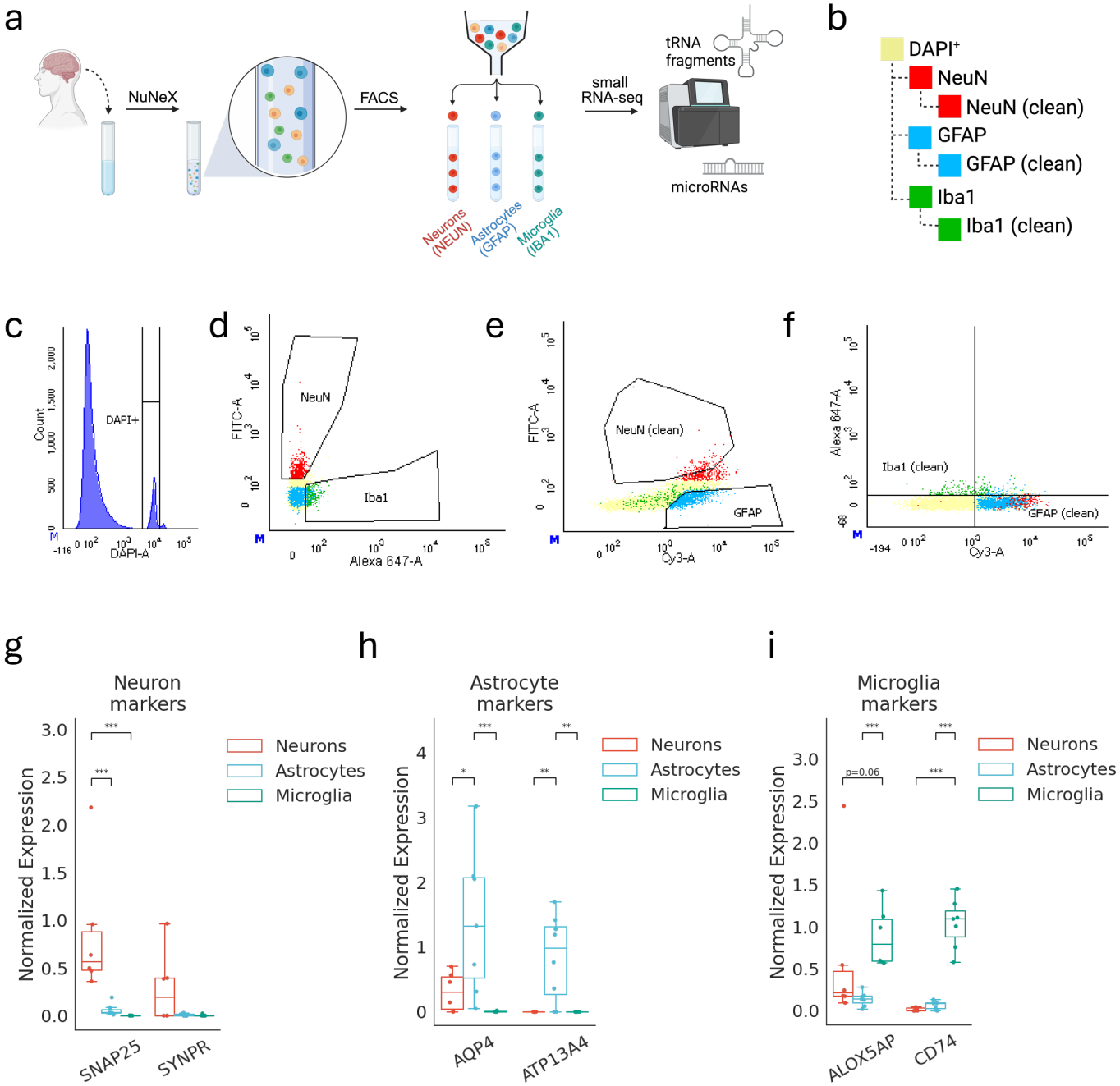
a
NuNeX
FACS
small RNA-seq
tRNA fragments
microRNAs
Neurons (NEUN)
Astrocytes (GFAP)
Microglia (IBA1)
b
DAPI+
NeuN
NeuN (clean)
GFAP
GFAP (clean)
Iba1
Iba1 (clean)
c
Count
DAPI+
DAPI-A
d
FITC-A
NeuN
Iba1
Alexa 647-A
e
FITC-A
NeuN (clean)
GFAP
Cy3-A
f
Alexa 647-A
Iba1 (clean)
GFAP (clean)
Cy3-A
g
Neuron markers
Normalized Expression
Neurons
Astrocytes
Microglia
SNAP25
SYNPR
h
Astrocyte markers
Normalized Expression
Neurons
Astrocytes
Microglia
AQP4
ATP13A4
i
Microglia markers
Normalized Expression
Neurons
Astrocytes
Microglia
p=0.06
ALOX5AP
CD74

Figure 2

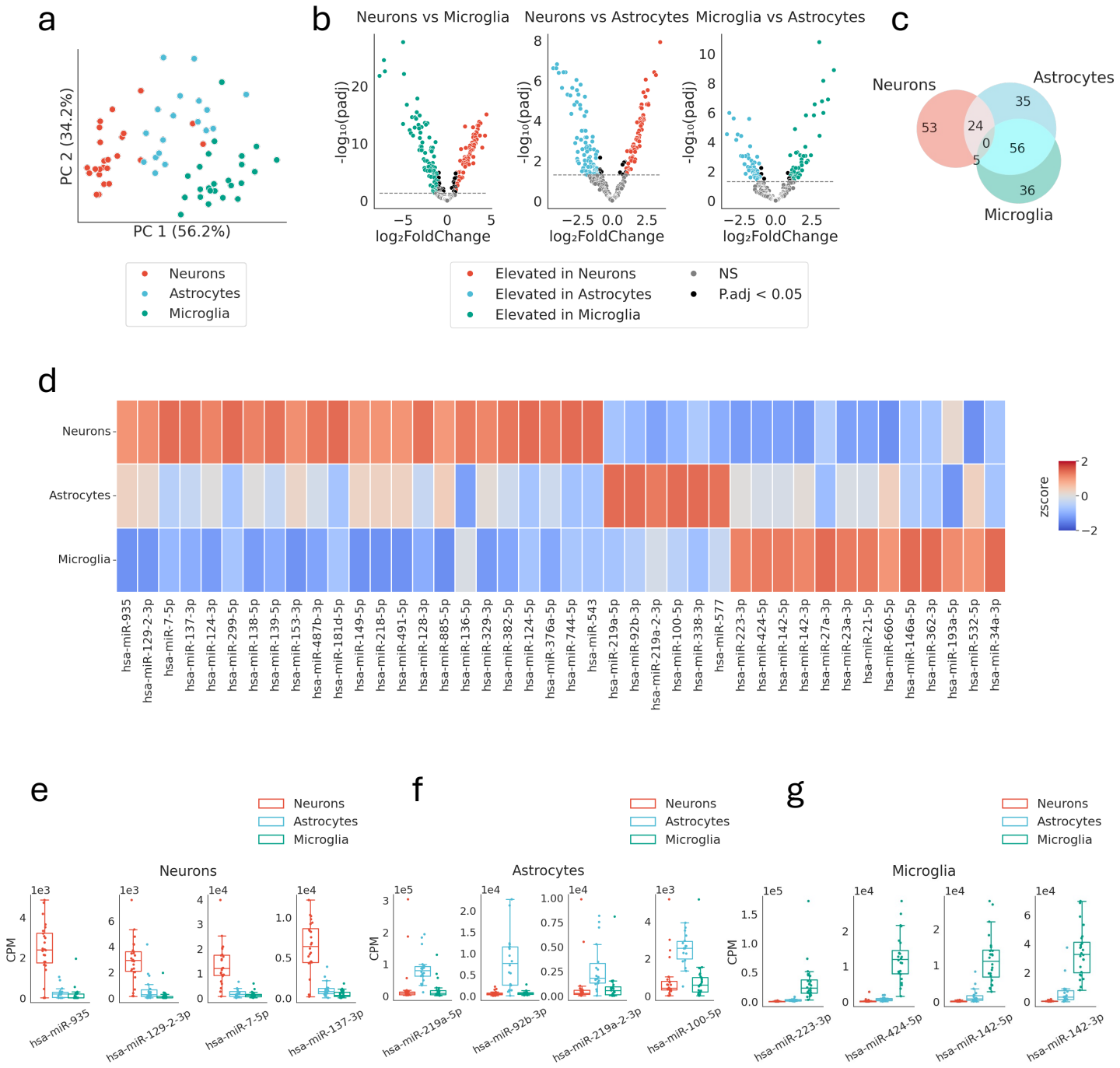
a
PC 2 (34.2%)
PC 1 (56.2%)
Neurons
Astrocytes
Microglia
b
Neurons vs Microglia
Neurons vs Astrocytes
Microglia vs Astrocytes
-log10(padj)
log2FoldChange
Elevated in Neurons
Elevated in Astrocytes
Elevated in Microglia
NS
P.adj < 0.05
c
Neurons
Astrocytes
Microglia
53
24
35
0
56
5
36
d
Neurons
Astrocytes
Microglia
zscore
hsa-miR-935
hsa-miR-129-2-3p
hsa-miR-7-5p
hsa-miR-137-3p
hsa-miR-124-3p
hsa-miR-299-5p
hsa-miR-138-5p
hsa-miR-139-5p
hsa-miR-153-3p
hsa-miR-487b-3p
hsa-miR-181d-5p
hsa-miR-149-5p
hsa-miR-218-5p
hsa-miR-491-5p
hsa-miR-128-3p
hsa-miR-885-5p
hsa-miR-136-5p
hsa-miR-329-3p
hsa-miR-382-5p
hsa-miR-124-5p
hsa-miR-376a-5p
hsa-miR-744-5p
hsa-miR-543
hsa-miR-219a-5p
hsa-miR-92b-3p
hsa-miR-219a-2-3p
hsa-miR-100-5p
hsa-miR-338-3p
hsa-miR-577
hsa-miR-223-3p
hsa-miR-424-5p
hsa-miR-142-5p
hsa-miR-142-3p
hsa-miR-27a-3p
hsa-miR-23a-3p
hsa-miR-21-5p
hsa-miR-660-5p
hsa-miR-146a-5p
hsa-miR-362-3p
hsa-miR-193a-5p
hsa-miR-532-5p
hsa-miR-34a-3p
e
Neurons
Astrocytes
Microglia
CPM
hsa-miR-935
hsa-miR-129-2-3p
hsa-miR-7-5p
hsa-miR-137-3p
f
Astrocytes
hsa-miR-219a-5p
hsa-miR-92b-3p
hsa-miR-219a-2-3p
hsa-miR-100-5p
g
Microglia
hsa-miR-223-3p
hsa-miR-424-5p
hsa-miR-142-5p
hsa-miR-142-3p

Figure 3

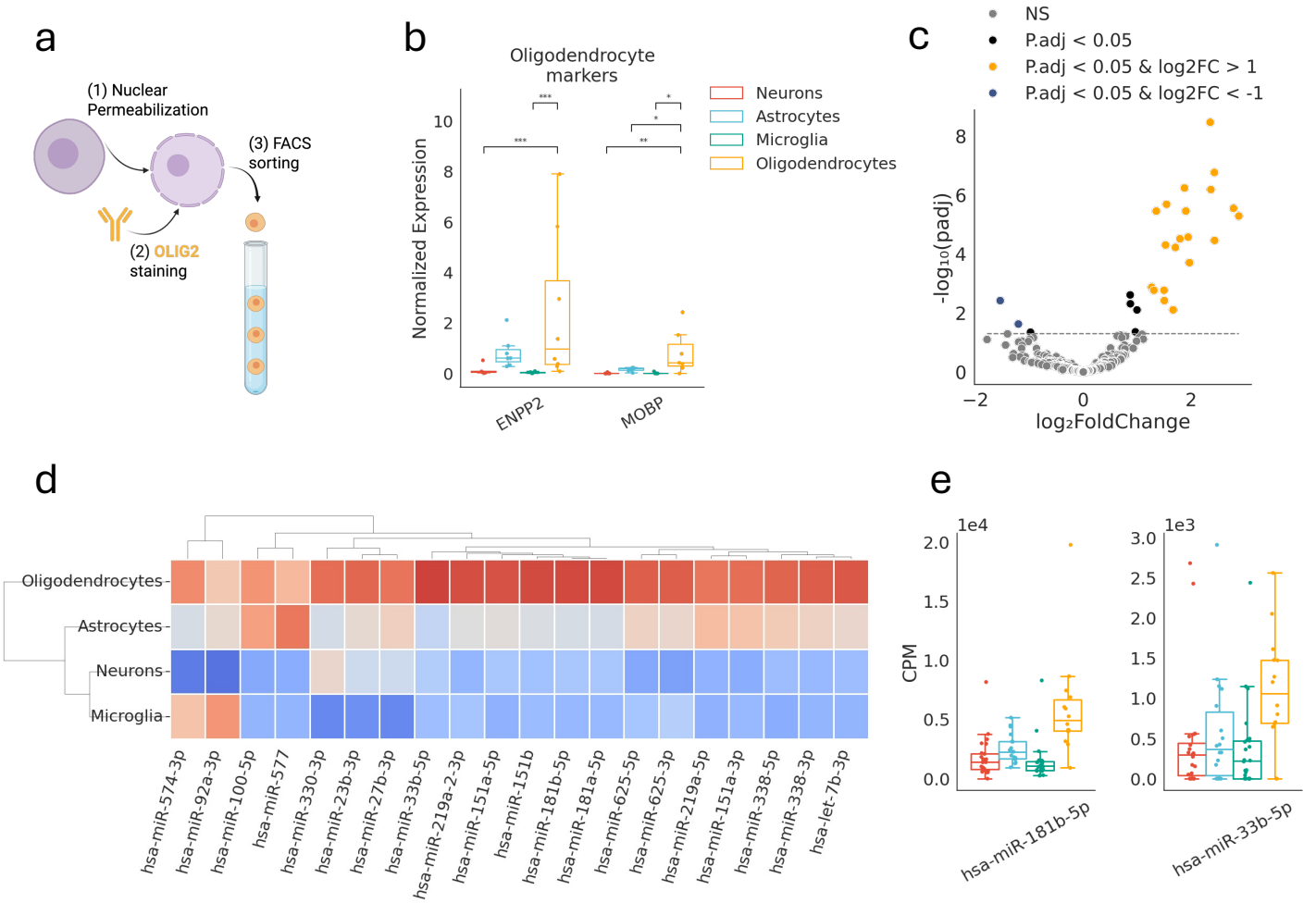
a
(1) Nuclear Permeabilization
(2) OLIG2 staining
(3) FACS sorting
b
Oligodendrocyte markers
Normalized Expression
Neurons
Astrocytes
Microglia
Oligodendrocytes
ENPP2
MOBP
c
NS
P.adj < 0.05
P.adj < 0.05 & log2FC > 1
P.adj < 0.05 & log2FC < -1
-log10(padj)
log2FoldChange
d
Oligodendrocytes
Astrocytes
Neurons
Microglia
hsa-miR-574-3p
hsa-miR-92a-3p
hsa-miR-100-5p
hsa-miR-577
hsa-miR-330-3p
hsa-miR-23b-3p
hsa-miR-27b-3p
hsa-miR-33b-5p
hsa-miR-219a-2-3p
hsa-miR-151a-5p
hsa-miR-151b
hsa-miR-181b-5p
hsa-miR-181a-5p
hsa-miR-625-5p
hsa-miR-625-3p
hsa-miR-219a-5p
hsa-miR-151a-3p
hsa-miR-338-5p
hsa-miR-338-3p
hsa-let-7b-3p
e
CPM
1e4
1e3
hsa-miR-181b-5p
hsa-miR-33b-5p

Figure 4

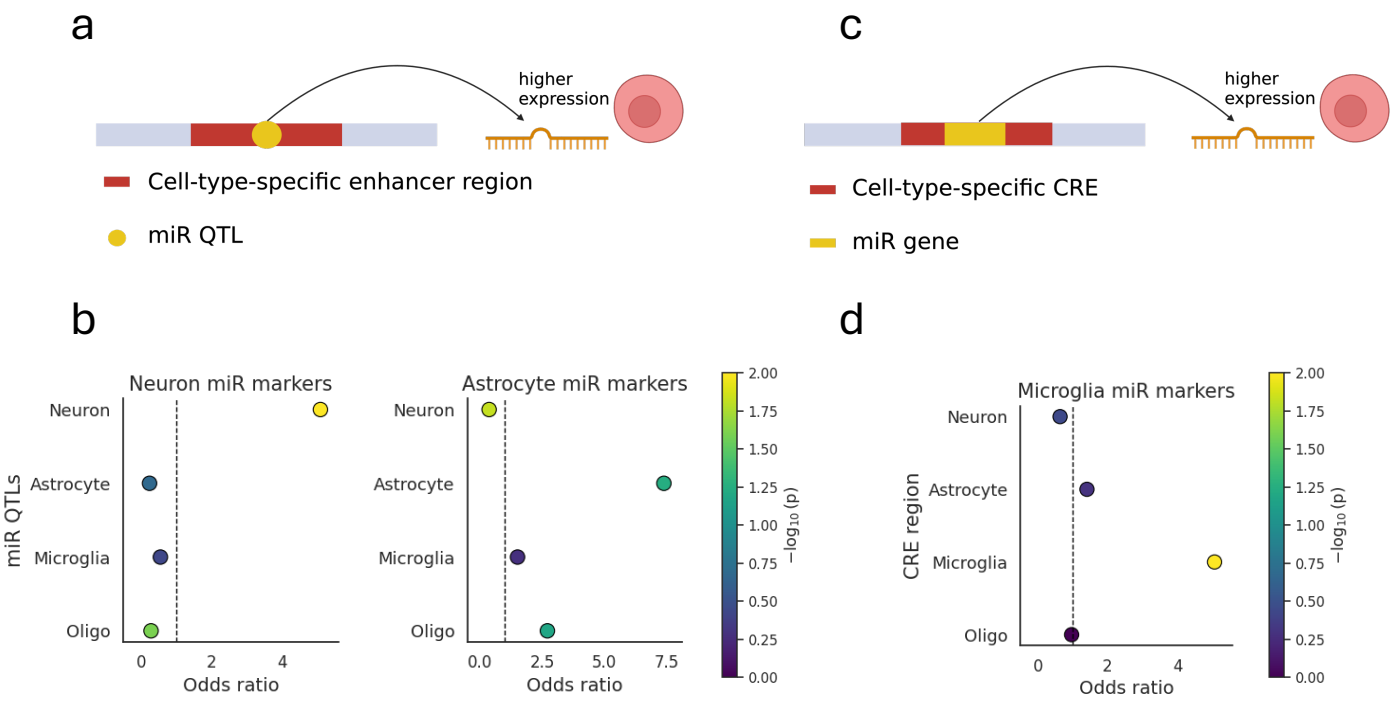
a
higher expression
Cell-type-specific enhancer region
miR QTL
c
higher expression
Cell-type-specific CRE
miR gene
b
Neuron miR markers
Astrocyte miR markers
miR QTLs
Neuron
Astrocyte
Microglia
Oligo
0
2
4
0.0
2.5
5.0
7.5
Odds ratio
2.00
1.75
1.50
1.25
1.00
0.75
0.50
0.25
0.00
−log10 (p)
d
Microglia miR markers
CRE region
Neuron
Astrocyte
Microglia
Oligo
0
2
4
Odds ratio
2.00
1.75
1.50
1.25
1.00
0.75
0.50
0.25
0.00
−log10 (p)

Figure 5

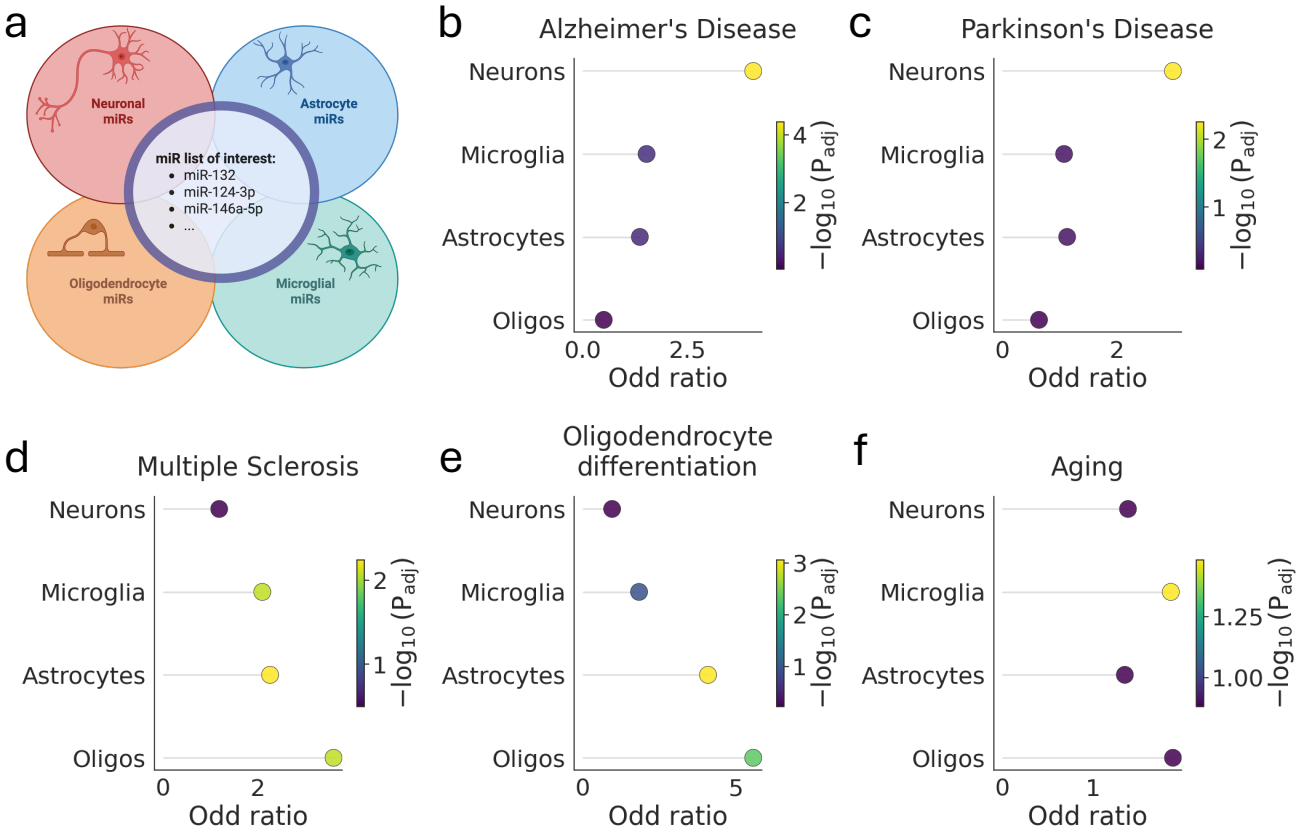
a
Neuronal miRs
Astrocyte miRs
miR list of interest:
miR-132
miR-124-3p
miR-146a-5p
...
Oligodendrocyte miRs
Microglial miRs
b
Alzheimer's Disease
Neurons
Microglia
Astrocytes
Oligos
0.0
2.5
Odd ratio
4
2
−log10 (Padj)
c
Parkinson's Disease
Neurons
Microglia
Astrocytes
Oligos
0
2
Odd ratio
2
1
−log10 (Padj)
d
Multiple Sclerosis
Neurons
Microglia
Astrocytes
Oligos
0
2
Odd ratio
2
1
−log10 (Padj)
e
Oligodendrocyte differentiation
Neurons
Microglia
Astrocytes
Oligos
0
5
Odd ratio
3
2
1
−log10 (Padj)
f
Aging
Neurons
Microglia
Astrocytes
Oligos
0
1
Odd ratio
1.25
1.00
−log10 (Padj)

Figure 6

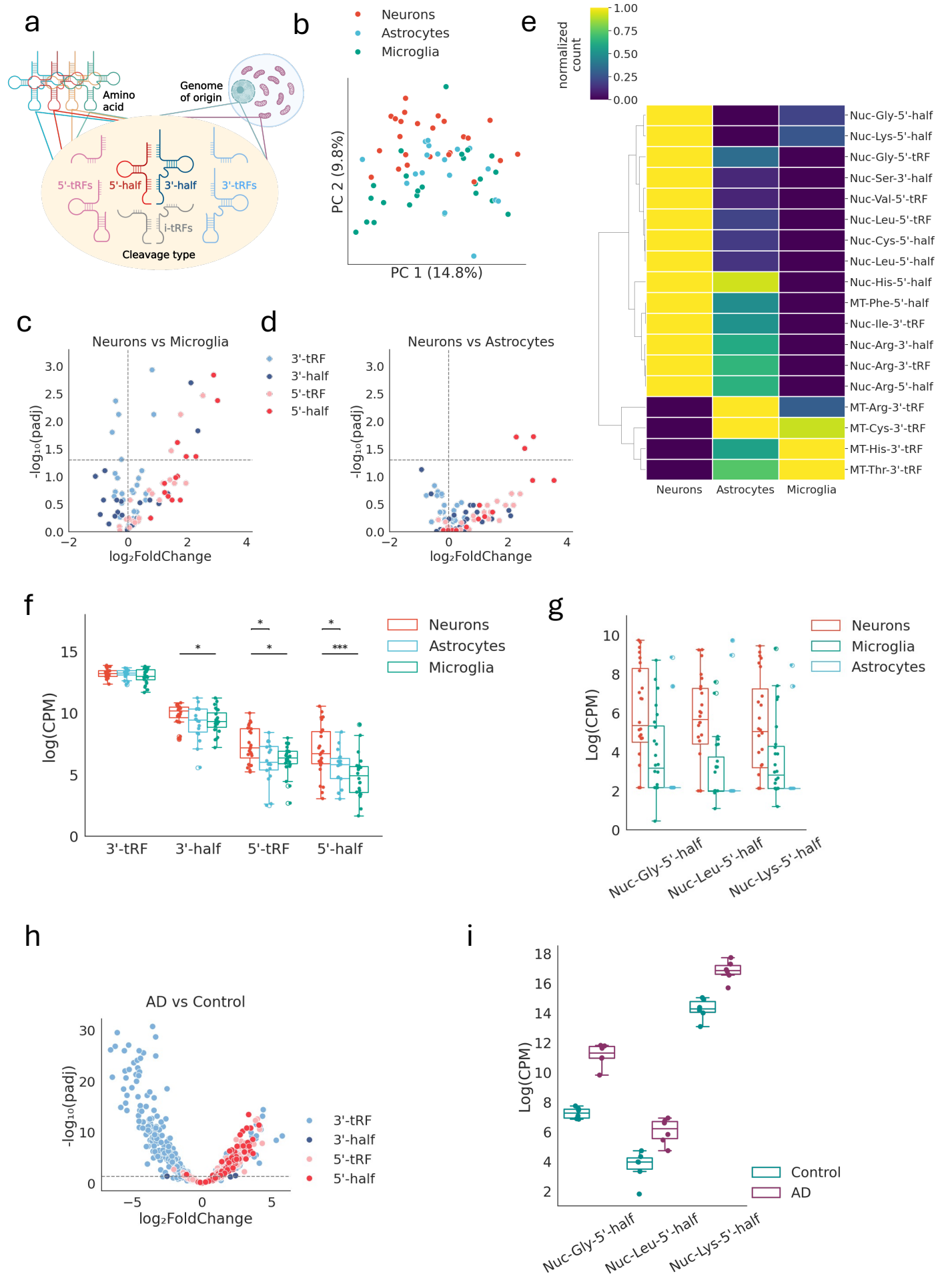
a
Amino acid
Genome of origin
5'-tRFs
5'-half
3'-half
3'-tRFs
i-tRFs
Cleavage type
b
Neurons
Astrocytes
Microglia
PC 2 (9.8%)
PC 1 (14.8%)
e
normalized count
1.00
0.75
0.50
0.25
0.00
Nuc-Gly-5'-half
Nuc-Lys-5'-half
Nuc-Gly-5'-tRF
Nuc-Ser-3'-half
Nuc-Val-5'-tRF
Nuc-Leu-5'-tRF
Nuc-Cys-5'-half
Nuc-Leu-5'-half
Nuc-His-5'-half
MT-Phe-5'-half
Nuc-Ile-3'-tRF
Nuc-Arg-3'-half
Nuc-Arg-3'-tRF
Nuc-Arg-5'-half
MT-Arg-3'-tRF
MT-Cys-3'-tRF
MT-His-3'-tRF
MT-Thr-3'-tRF
Neurons
Astrocytes
Microglia
c
Neurons vs Microglia
-log10(padj)
log2FoldChange
d
Neurons vs Astrocytes
3'-tRF
3'-half
5'-tRF
5'-half
-log10(padj)
log2FoldChange
f
Neurons
Astrocytes
Microglia
log(CPM)
3'-tRF
3'-half
5'-tRF
5'-half
g
Neurons
Microglia
Astrocytes
Log(CPM)
Nuc-Gly-5'-half
Nuc-Leu-5'-half
Nuc-Lys-5'-half
h
AD vs Control
-log10(padj)
log2FoldChange
3'-tRF
3'-half
5'-tRF
5'-half
i
Log(CPM)
Control
AD
Nuc-Gly-5'-half
Nuc-Leu-5'-half
Nuc-Lys-5'-half

Main Figure Legends

Figure 1. FACS sorting of neurons, astrocytes and microglia from live human brain tissue. a) Graphical representation of the pipeline used to produce the cell-type-resolved resource of small non-coding RNAs from live human brain. Created with BioRender. b) Scheme showing the FACS gate hierarchy: the primary parent gate is a DAPI-positive population; next, each cell-type-specific cellular population was identified via double gating, accessing its overlap with the two other cell types. Thus, NeuN-, GFAP-, and IBA1-positive gates included the refined daughter gates Neun-clean, GFAP-clean, and IBA1-clean. c) Histogram featuring the DAPI signal of FACS events, showing the defined DAPI-positive gate, separating single cells (middle peak) from debris (left peak, low signal levels) and doublets (right peak, higher signal level). d) Scatter plot showing Alexa 647 (IBA1) and FITC (NeuN) signals of the FACS events from the DAPI-positive gate shown in (c), with NeuN- and IBA1-positive gates. e) Scatter plot showing Cy3 (GFAP) and FITC (NeuN) signals of the DAPI-positive FACS events, with the refined NeuN-clean gate and GFAP-positive primary gate. f) Scatter plot showing the Cy3 (GFAP) and Alexa 647 (IBA1) signals of DAPI-positive FACS events, with the refined Iba1-clean and GFAP-clean gates ensuring minimal mutual overlap. g) Box plot showing qPCR-determined levels of SNAP25 and SYNPR in all three cell types, with neuronal levels set as controls. h) Box plot as in h for the astrocyte biomarkers AQP4 and ATP13A4, with astrocyte values set as controls. i) Box plot as in h for the microglial biomarkers ALOX5AP and CD74, with microglia values set as controls. All values were normalized to GAPDH and ACTB transcripts. Outliers were removed for each gene's cell type box using the standard boxplot definition, excluding values lying below Q1 – 1.5×IQR or above Q3 + 1.5×IQR. *$p \leq 0.05$, **$p \leq 0.01$, ***$p \leq 0.001$; values with $0.05 < p < 0.15$ are labeled.

Figure 2. Cell-type-specificity of brain miRs. a) Scatter plot of Principal Component Analysis (PCA) applied to miR profiles of cell-type-specific populations. b) Volcano plots showing dream pairwise DE analysis, comparing each pair of cell types. c) Venn diagram showing the overlaps between the elevated miRs in each cell type. d) Heatmap of mean cell type z-scores of marker miRs for each cell type, defined as significantly DE miRs with a log-fold change greater than 2, relative to both other cell types (Methods). e) Box plot showing expression levels of the top five neuron-enriched miRs (Methods). f) Box plot as in f for astrocyte-enriched miRs. g) Box plot as in f for microglia-enriched miRs.

Figure 3. Identification of oligodendrocyte-enriched miRs. a) Graphical representation of the FACS sorting pipeline used to isolate oligodendrocytes from live human brain specimens. Created with BioRender. b) qPCR-measured levels of ENPP2 and MOBP, normalized to GADPH and ACTB transcripts, with oligodendrocyte levels set as controls. Outliers were removed within each gene's cell type box using the standard box plot definition, excluding values lying below Q1 – 1.5×IQR or above Q3 + 1.5×IQR. *$p \leq 0.05$, **$p \leq 0.01$, ***$p \leq 0.001$. c) Volcano plot showing the DE result, comparing the oligodendrocyte miR signature to other cell type populations. d) Heatmap showing z-scores of 20 miRs, significantly elevated in oligodendrocytes (log2 fold change > 1, adjusted $p \leq 0.05$), compared to all other cell types. e) Boxplots showing the levels of two oligodendrocyte marker miRs (log2 fold change > 2; adjusted $p \leq 0.05$; Methods). CPM - counts per million.

Figure 4. Cell-type-specific miRs are associated with cell-type-specific regulatory elements. a) Schematic representation of a miR-QTL (yellow) residing within a cell-type-specific enhancer region (red), thereby contributing to the cell-type-specific expression of associated miRs. Created with BioRender. b) Dot plots showing Fisher's exact test results (alternative = two-sided) for the association between miRs enriched in neurons (left) and in astrocytes (right), and the associated miR-QTLs residing within cell-type-specific enhancer regions. Y-axis depicts cell type, X-axis positions reflect the odds ratio of each association, and dot colors depict $-\log_{10}$ p-values (unadjusted). c) Schematic representation of a miR gene (yellow) located within a cell-type-specific cis regulatory

element (CRE) (red) that contributes to cell-type-specific expression of the miR. Created with BioRender. d) Dot plot showing Fisher's exact test results (alternative = two-sided) for the association between miRs enriched in microglia and the cell-type-specific cis-regulatory elements (CREs). Y-axis depicts cell type, X-axis positions reflect the odds ratio of each association, and dot colors depict -$\log_{10}$ p-values (unadjusted).

Figure 5. Measuring cell type enrichment in miR lists of interest. a) Graphical representation of the pipeline used to deconvolve miR lists of interest to specific cell type signals. Cell-type enrichment for a given list is calculated by applying the Fisher's exact test to the overlaps between the cell type miR markers, identified in this study, and the input miR list. Thus, every analysis consists of four independent statistical tests (for the association with each of the four cell types), corrected for multiple comparisons. Created with BioRender. b-f) Fisher's exact test (*alternative* = *greater*) results for deconvolution of (b) AD[64], (c) PD[65], (d) MS[66], (e) oligodendrocyte differentiation[68] and (f) brain aging[69] miR signatures. Reported *p*-values were adjusted for multiple testing using false discovery rate control.

Figure 6. Cell-type specificity of tRF families. a) Graphical representation of the three elements defining tRF families. Created with BioRender. b) Scatter plot of Principal Component Analysis (PCA) applied to tRF family profiles of the three cell populations. c-d) Volcano plots showing the tRF family DE analysis, colored by tRFs cleavage type, comparing (c) neuronal and microglial profiles; and (d) neuronal and astrocytic profiles. e) Heatmap showing the mean normalized scores of statistically significant tRF families across three distinct cell type populations. f) Box plot of the patient-wise average levels of tRF families, grouped by cleavage type. Significance was determined using the Mann-Whitney non-parametric test. *$p \leq 0.05$, **$p \leq 0.01$, ***$p \leq 0.001$. g) Same as (f) showing the levels of tRF families upregulated in neurons compared to astrocytes and microglia, grouped by cleavage type and amino acid. h) Volcano plot showing DE analysis of AD samples vs. healthy age-matched controls, colored by tRF cleavage type. i) Box plot showing expression levels of neuron-enriched tRF families in AD samples and age-matched controls.

Supplementary Figure 1

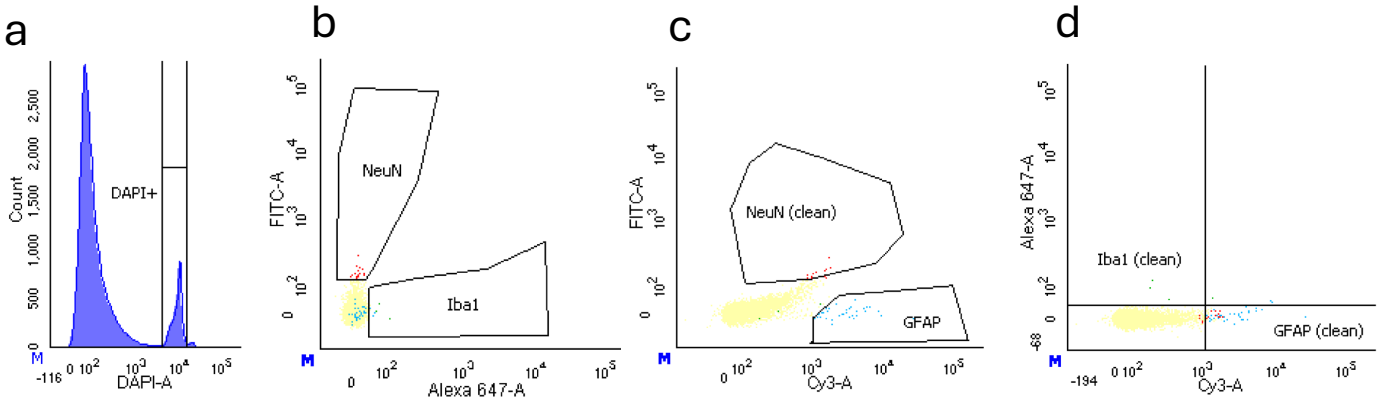

e Tube: NC

Population	#Events	%Parent	%Total
All Events	100,000	####	100.0
Scatter gate	91,466	91.5	91.5
SSC	90,209	98.6	90.2
FSC	90,196	100.0	90.2
DAPI+	10,244	11.4	10.2
NeuN	15	0.1	0.0
Q1-2	8	53.3	0.0
Q2-2	7	46.7	0.0
Q3-2	0	0.0	0.0
Q4-2	0	0.0	0.0
NeuN (clean)	8	53.3	0.0
Iba1	5	0.0	0.0
Iba1 (clean)	2	40.0	0.0
Q2-1	3	60.0	0.0
Q3-1	0	0.0	0.0
Q4-1	0	0.0	0.0
GFAP	35	0.3	0.0
Q1-3	0	0.0	0.0
Q2-3	2	5.7	0.0
Q3-3	0	0.0	0.0
GFAP (clean)	33	94.3	0.0

f Tube: TEST

Population	#Events	%Parent	%Total
All Events	67,273	####	100.0
Scatter gate	61,967	92.1	92.1
SSC	61,327	99.0	91.2
FSC	61,308	100.0	91.1
DAPI+	5,691	9.3	8.5
NeuN	438	7.7	0.7
Q1-2	2	0.5	0.0
Q2-2	436	99.5	0.6
Q3-2	0	0.0	0.0
Q4-2	0	0.0	0.0
NeuN (clean)	115	26.3	0.2
Iba1	249	4.4	0.4
Iba1 (clean)	95	38.2	0.1
Q2-1	138	55.4	0.2
Q3-1	7	2.8	0.0
Q4-1	9	3.6	0.0
GFAP	960	16.9	1.4
Q1-3	0	0.0	0.0
Q2-3	80	8.3	0.1
Q3-3	4	0.4	0.0
GFAP (clean)	876	91.2	1.3

Supplementary Figure 2

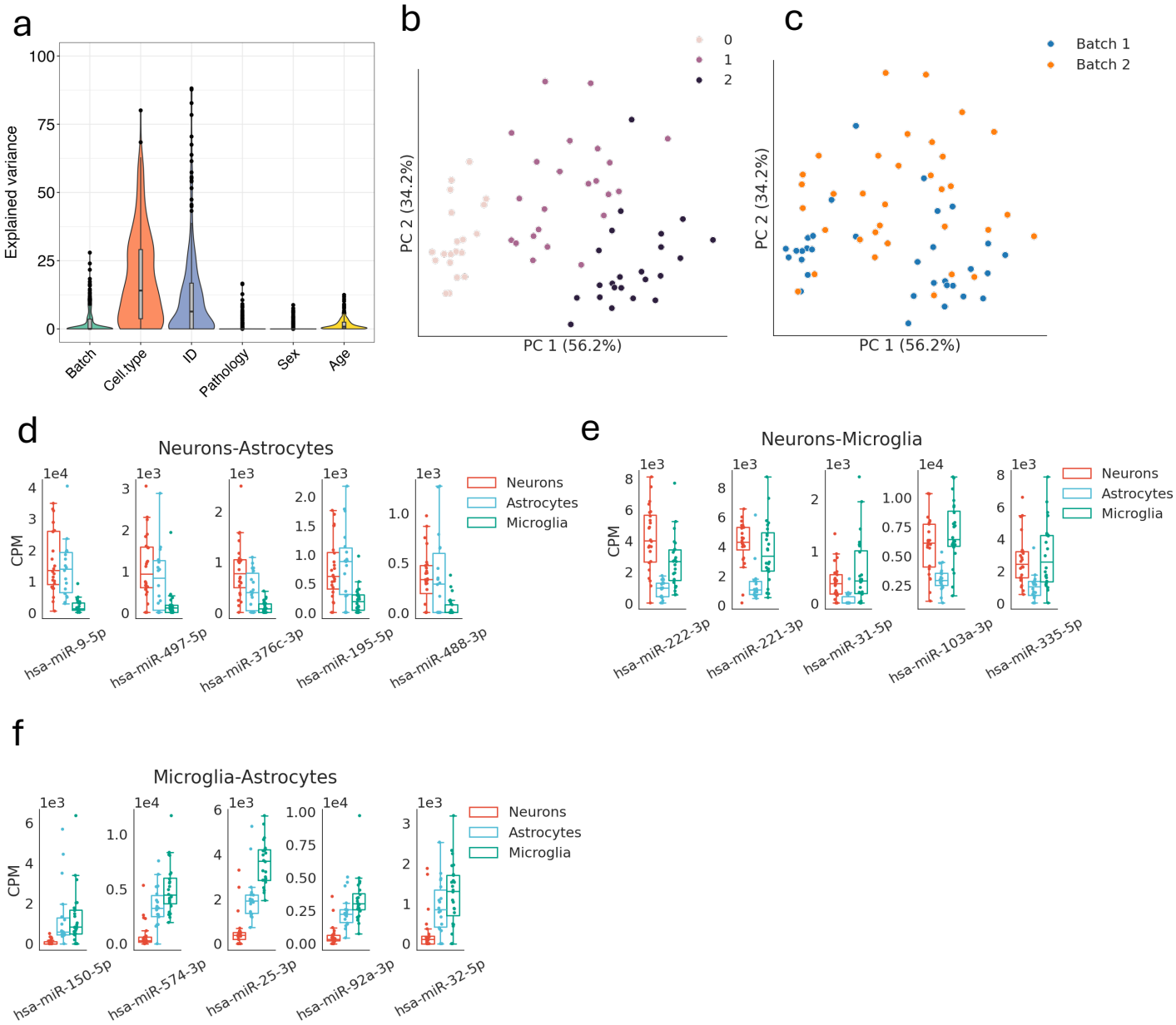

Supplementary Figure 3

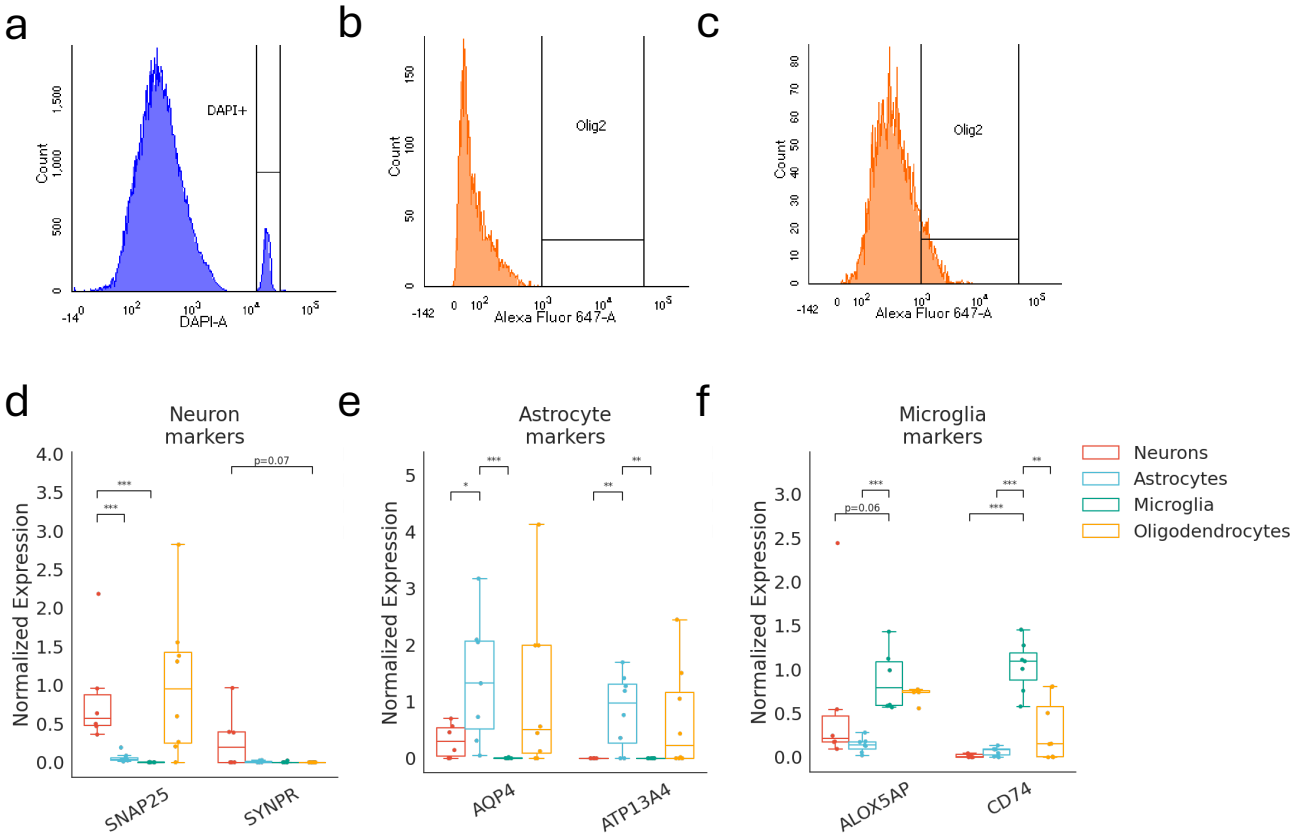

Supplementary Figure 4

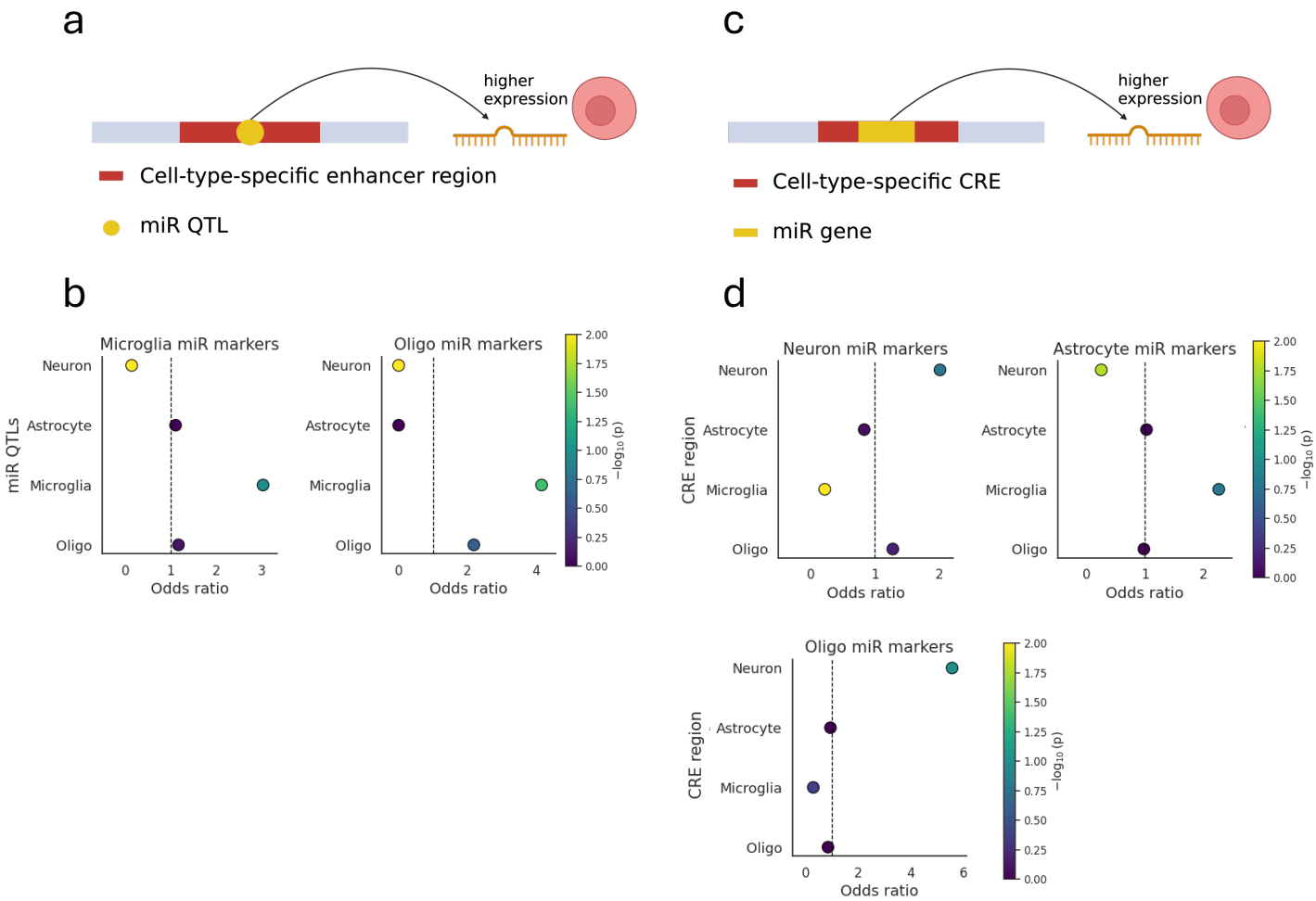

Supplementary Figure 5

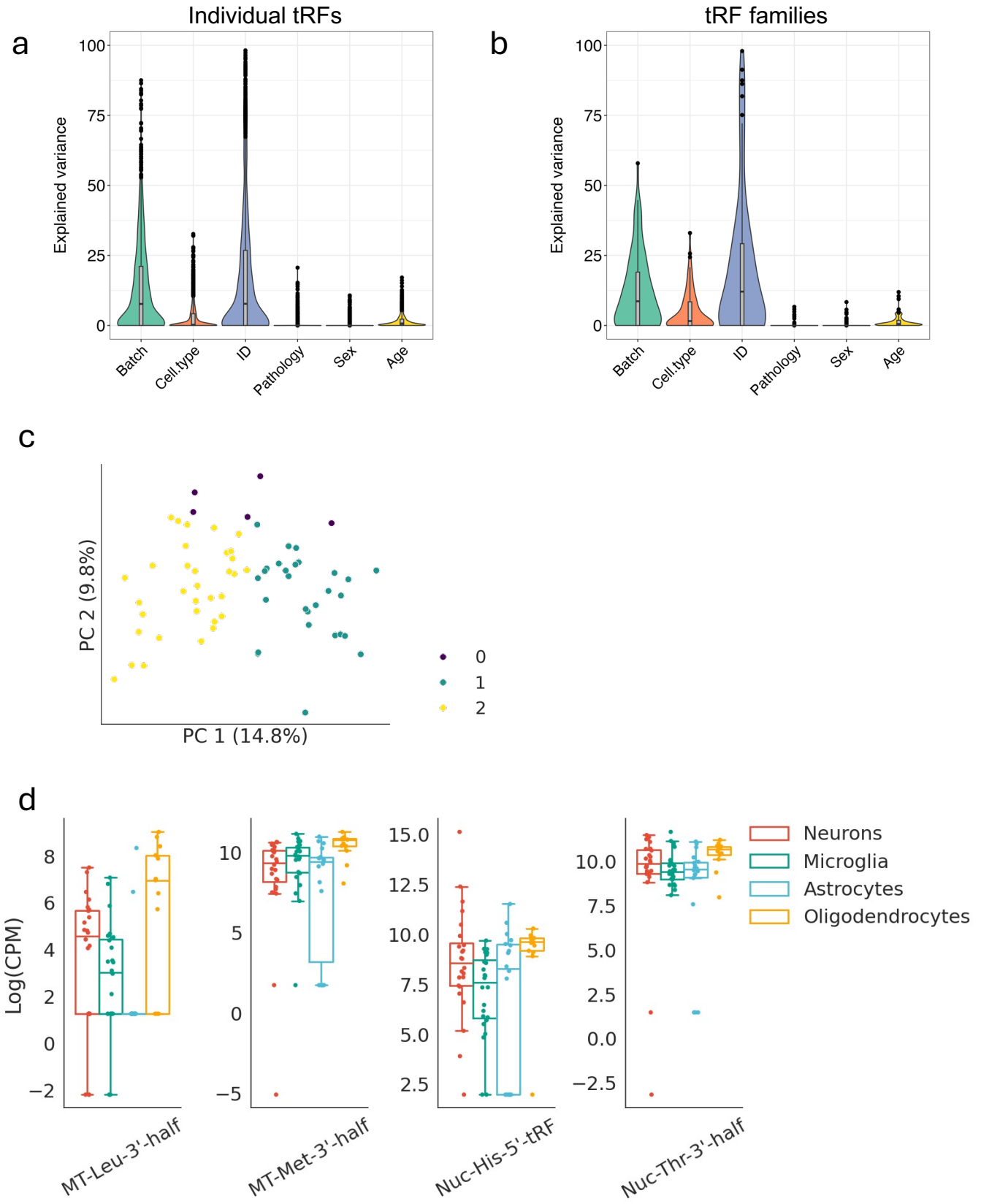

Supplementary Figure Legends

Supplementary Figure 1. a) Histogram of DAPI fluorescence for FACS events in a representative negative Control (NC) sample stained with DAPI only. b) Scatter plot showing Alexa 647 (IBA1) vs. FITC (NeuN) signals for FACS events in the NC sample stained with DAPI only. c) Scatter plot showing Cy3 (GFAP) vs. FITC (NeuN) signals for DAPI-positive FACS events in the NC sample stained with DAPI only. d) Scatter plot of Cy3 (GFAP) versus Alexa 647 (IBA1) signals for DAPI-positive gated events in the NC sample, showing refined IBA1-clean and GFAP-clean gates with minimal mutual overlap. e) FACS table quantifying the proportions of events assigned to each gate in the NC sample. f) Same as (e) for the Test sample shown in Main Figure c–f.

Supplementary Figure 2. a) Violin plot generated with the *variancePartition* package, showing the proportion of explained variance in miR expression profiles attributed to Batch, Cell type, Patient ID, Pathology (meningioma/metastasis), Sex, and Age. b) PCA of miR expression profiles colored by k-means cluster assignments. c) PCA of miR expression profiles colored by Batch. d) Box plots of the top five miRs (ranked by mean log fold change) significantly elevated in both neurons and astrocytes relative to microglia. e) Box plots of the top five miRs significantly elevated in both neurons and microglia relative to astrocytes. f) Boxplots of the top five miRs significantly elevated in both microglia and astrocytes relative to neurons.

Supplementary Figure 3. a) Histogram of DAPI fluorescence for FACS events in a representative sample stained with DAPI and OLIG2 for oligodendrocyte sorting. b) Histogram of Alexa 647 (OLIG2) fluorescence in a representative NC sample stained with DAPI only. c) Same as (b) for the same sample stained with both DAPI and OLIG2. d) Box plots showing normalized expression of neuronal markers *SNAP25* and *SYNPR* across sorted populations (neurons, astrocytes, microglia, and oligodendrocytes), determined by qPCR. e) Same as (d) for astrocyte markers *AQP4* and *ATP13A4*. f) Same as (d) for microglia markers *ALOX5AP* and *CD74*. Outliers were removed per gene and cell type using the standard boxplot definition (values below Q1 − 1.5×IQR or above Q3 + 1.5×IQR). *$p \leq 0.05$, **$p \leq 0.01$, ***$p \leq 0.001$; values with $0.05 < p < 0.15$ are labeled.

Supplementary Figure 4. a) Schematic representation of a miR-QTL residing in a cell-type-specific enhancer region, contributing to the cell-type-specific expression of the associated miR. Created with BioRender. b) Dot plots showing Fisher's exact test results (alternative = two-sided) for the association between miRs enriched in microglia (left) and oligodendrocytes (right), and the associated miR-QTLs residing in cell-type-specific enhancer regions. Y-axis depicts cell type, X-axis positions reflect the odds ratio of each association, and dot colors depict $-\log_{10}$ p-values (unadjusted). c) Schematic representation of a miR gene located within a cell-type-specific cis regulatory element (CRE) (red) that contributes to cell-type-specific expression of the miR.. Created with BioRender. d) Dot plots showing Fisher's exact test results (alternative = two-sided) for associations between transcriptomically enriched miRs in neurons (top left), astrocytes (top right), and oligodendrocytes (bottom left), and miRs residing within cell-type-specific cis-regulatory elements (CRE). Y-axis depicts cell type, X-axis positions reflect the odds ratio of each association, and dot colors depict $-\log_{10}$ p-values (unadjusted).

Supplementary Figure 5. a) Violin plot generated with the *variancePartition* package, showing explained variance in individual tRF expression profiles attributable to Batch (0.135), Cell type (0.031), Patient ID (0.181), Pathology (0.005), Sex (0.004), and Age (0.017). b) Violin plot showing explained variance in tRF family expression profiles attributable to Batch (0.121), Cell type (0.051), Patient ID (0.204), Pathology

(0.004), Sex (0.005), and Age (0.016). c) PCA of tRF family expression profiles colored by k-means cluster assignment. d) Box plot of tRF families significantly elevated in oligodendrocytes compared to all other cell types (Mann–Whitney test; all shown families have adjusted $p < 0.05$).